Physical Origin of Hyperuniformity in Epithelial Tissue

---

by

Jakob Sheridan

Research Advisor:

David K. Lubensky

TABLE OF CONTENTS

ABSTRACT

Epithelia are quasi-two-dimensional sheets of cells that play an important role in the early developmental processes of many types of animal tissue. The dynamics of these tissues depend on the spatial structure of the cells, which interact and generate mechanical forces amongst one another in complex ways. An epithelium is an active disordered material, meaning the study of its structural features lack the symmetry or elegance of that allowed by crystallography, limiting the tools at one's disposal to fully describe the relationship between cellular arrangement and the resultant forces at work.

Here, we apply a vertex model framework to represent epithelia and develop an understanding of the spatial distribution of cells produced by it. We observe evidence of hyperuniformity exhibited by the simulations, characterized by the suppression of density fluctuations at long length scales, often referred to as a form of "hidden order" in nature. The computational methods employed to produce these results are discussed, as well as the limitations that prevent a full exploration of this behavior. We present results relating the presence of hyperuniformity to the ratio between the bulk and shear moduli of the tissues, to explain this behavior with respect to measurable quantities outside the scope of simulation parameters.

The vertex model is meant to generalize to any physical or theoretical system describing epithelia, and we demonstrate this by comparing data from simulations to a theoretical continuum model that predicts the dynamics of elastic tissues featuring noisy growth and mechanical feedback. We focus on findings for the statistics of marked, neutral clones and verify the prediction that the normalized variance of clone areas scale like the inverse of the initial size of the clone. Other analytic results concerning the time-dependent behavior of clone size variance disagree with simulation data and suggest evidence of the vertex model exhibiting nonlinear behavior related to hyperuniformity.

We discuss the development of new models to capture the relationship between density fluctuations in disordered systems and its elastic properties. The results presented throughout the thesis lay a groundwork for future projects in pursuit of understanding the origin of hyperuniformity in the vertex model and disordered systems in general.

CHAPTER I
Introduction

Communicating the details with which epithelial cells coordinate themselves into complex biological structures can lead to fascinating discussions and insights. Exploring this topic from a physics standpoint can reveal even more interesting behavior providing a unique understanding of the mechanisms and properties that drive development. This chapter will serve as a general introduction to important concepts at the focal point of the thesis. To preface the results of subsequent chapters, a brief biological overview of epithelia will be provided, alongside an initial introduction to the vertex model used to produce computational simulations. We will then discuss ideas from elasticity theory, as these will be used often to relate our discretized cell models of epithelia to the well-defined properties of continuous elastic materials. Finally, hyperuniformity in disordered systems will be given a thorough treatment, as this phenomenon is the focus for most of our findings.

1.1 Epithelium

Epithelium is one of the primary types of animal tissue organisms use to build complex tissues and organs during development [1, 2, 3, 4]. This tissue can be thought of as a quasi-two-dimensional array of cells that provide a protective alignment for the outer surfaces of organs and blood vessels, for example [5, 6, 7]. In particular, epithelial cells play an important role in developmental biology, which is typically divided into the processes controlling tissue growth, patterning of cellular differentiation, and morphogenesis. In this thesis, the focus is restricted to morphogenesis, which attempts to describe the process of how cells and tissue develop their shapes. The processes of a tissue determining its shape and spatial distribution of cells are involved not only during the embryonic stages of growth for an organism, but also in the study of stem cells and regeneration of damaged tissue. Cancer is also relevant example of abnormal morphogenetic behavior, and so understanding the underlying mechanics involved is an important topic of interest [8, 9, 10, 11].

Epithelia are an active material capable of both producing and reacting to mechanical forces. Tissue comprised of epithelial cells form a continuous sheet, with neighboring cells attached to each other through specialized protein complexes called adherens junctions. These adherens junctions ensure that the boundaries of each cell are bound tightly together and maintain the epithelium's mechanical integrity [12, 13]. Another feature of these cells influencing cell-cell interactions is a band of contractile cortical actomyosin underneath the adherens junctions that, in combination with one another, creates an effective line tension in each junction allowing cells to modulate the contractility of their borders. Altogether, these biological structures describing cell-cell adhesion and actomyosin cortical contractility introduce forces that cause cell shape change and the rearrangements that underlie morphogenetic processes [14, 15].

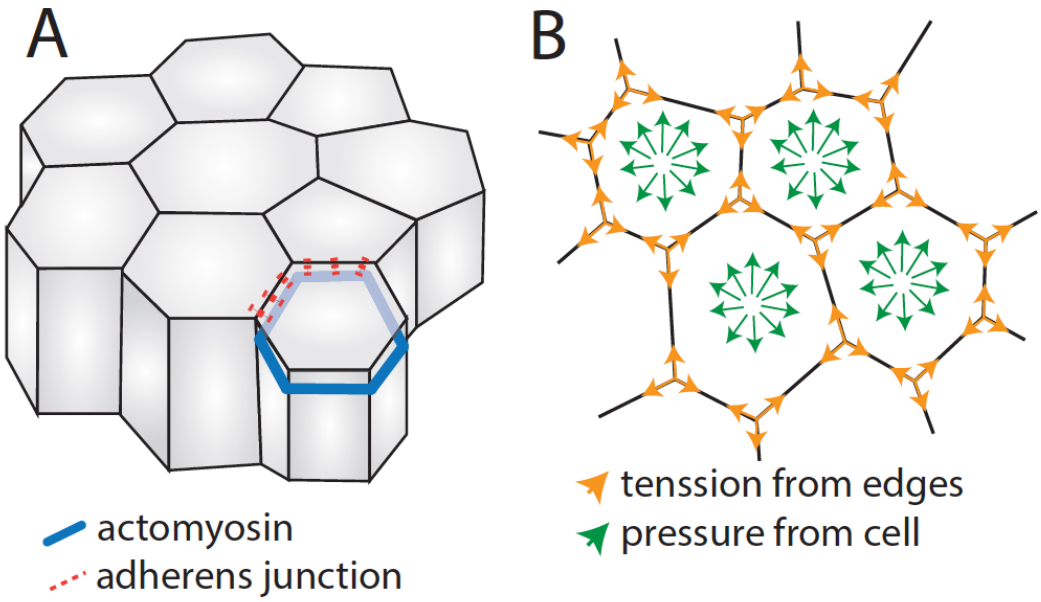

FIG. 1.1: **A** Cartoon example of an epithelium. Bands of actomyosin surrounding each cell create contractile forces. Adherens junctions maintain contact between cells. **B** Simple illustrative model of epithelium as a two-dimensional network of cells and edges. Tissue dynamics are determined by balancing forces between cell pressures and edge tensions. Original cartoon credited to Meryl Spencer [16].

There are three important topological changes that take place in epithelial tissue that drive morphogenesis: mitosis, apoptosis (or T2 transitions), and T1 transitions. Mitosis can be described as a singular cell dividing itself into two cells with identical properties. During mitosis, a cell is segmented along a random axis, and is the primary mechanism by which a tissue can grow [17]. Apoptosis is essentially the inverse of mitosis, in which a cell dies and is purged from the tissue. During apoptosis, a cell shrinks, and its neighboring cells move in to replace the subsequent gap to ensure that the extruded cell does not compromise the continuous nature of the tissue. T1 transitions, on the other hand, do not involve adding or removing cells from the tissue, acting instead as a more direct rearrangement of the cells in a tissue, shown in fig. 1.2. During a T1 transition, cells swap neighbors by shrinking the border between two cells until four are all adjacent to one site, after which the shrunken border elongates in a roughly perpendicular direction. T1 transitions cause a change in the topology of the tissue, allowing cells in the sheet to change shape and reach their preferred locations [18].

From the interplay between mechanical forces and cellular rearrangements described above, one can attempt to understand the behavior and mechanisms involved in morphogenetic processes through a biophysical lens. However, though the importance of cell structure and organization in epithelium is apparent, the biophysical mechanisms involved in describing the behavior of cell shape and position is still lacking. A further understanding of the physics underlying epithelium is required to build more reliable quantitative and predictive models of developmental processes in biological tissue.

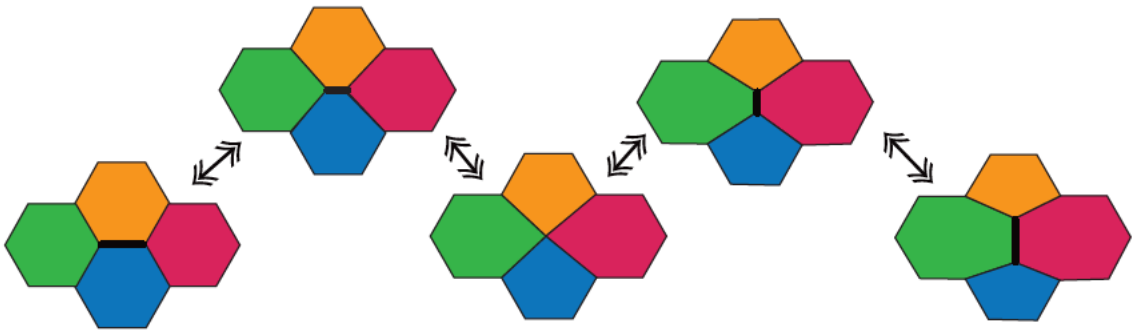

FIG. 1.2: Cartoon of a T1 transition. Neighbor exchange is caused by an edge shrinking until forming a fourfold vertex and then elongating again in the perpendicular direction. Original cartoon credited to Meryl Spencer [16].

This thesis focuses on expanding our understanding of the cellular mechanics and arrangement of epithelia using one of these predictive models. Given the complex dynamical behavior of biological tissue, it is necessary to utilize computational models to study their behavior in time [19, 20]. There are many types of models commonly used, though this thesis will deal exclusively with a vertex model. The vertex model reduces an epithelial sheet to a two-dimensional plane of points representing sites where three or more cells meet, connected by straight lines, or *edges*, as the junctions between neighboring cells. The degrees of freedom of such a model are these points, or *vertices*, which each experience forces imposed by equations of motion and integrated through time [21, 22, 23]. This model assigns forces on a cellular scale, ignoring the finer biological structures that grant the tissue its mechanical properties. However, the equations of motion imposed on each vertex are inspired by known biological components of the cell, such as a vertex subject to a contractile force from each of its edges just as a cell feels an effective tension from the cortical actomyosin bands along each of its boundaries [24].

A physical justification for using the vertex model as described is its similarity to a model of dry soap film, an array of bubbles with very little interstitial fluid separating the boundaries between them. The behavior of dry soap films is well defined mathematically, from research dating as far back as the 1800s by Plateau [18]. In modeling the evolution of a soap film, the final shape of each bubble is determined by minimizing the surface area of the bubble or length of its interfaces, dependent on some value of surface tension. Due to this interfacial tension influencing the dynamics of both soap films and epithelial tissue, models commonly used to describe these films have also been used to model the dynamics of epithelium. The vertex model is a simplified variant of these types of models, as it is restricted to two dimensions instead of three, and the edges representing cell boundaries are straight lines connecting vertices rather than having an arbitrary curvature as in the Plateau model. Despite these differences, the vertex model still adequately inherits the fundamental physics of the system due to epithelial cells' approximately polygonal shapes and has been applied to the study of epithelial morphogenesis in the past with positive results [21, 25, 26]. Simulations produced by the vertex model are featured prominently in the work detailed by this thesis and will be discussed further in Chapter II.

1.2 Linear Elasticity

Epithelium, as discussed above, is capable of generating complex internal forces and topological rearrangements that can cause complications when applying strategies from physics to develop models that try to predict its mechanical properties. Due to the quadratic energy cost imposed by our model penalizing deformations from a preferred area, as well as the assumption that significant displacement of cell positions occurs over long timescales, the dynamics of the tissue are often thought in terms of material properties like elasticity [27, 28]. An obvious first guess for a coarse-grained continuum model is linear elasticity, and we will find it useful throughout this thesis to compare the results of cell-based, vertex model simulations to the predictions of linear elastic theory, which we will review here [29, 30].

We will often borrow from formulations of elasticity theory when describing quantities like stress and deformations felt by the tissue. When confronted with some applied force, a material body is correspondingly deformed. The deformation of a body is defined mathematically by a displacement vector, $\boldsymbol{u}_i = \boldsymbol{x'}_i - \boldsymbol{x}_i$, which describes the distance traveled by a singular point by subtracting the position vector before deformation, $\boldsymbol{x}_i$, from the position vector after deformation, $\boldsymbol{x'}_i$. From this, one can define a tensor giving the change in an element of length in the material after deformation at any point, called the *strain tensor*,

$$u_{ik} = \frac{1}{2}\left(\frac{\partial \boldsymbol{u}_i}{\partial \boldsymbol{x}_k} + \frac{\partial \boldsymbol{u}_k}{\partial \boldsymbol{x}_i} + \frac{\partial \boldsymbol{u}_l}{\partial \boldsymbol{x}_i}\frac{\partial \boldsymbol{u}_l}{\partial \boldsymbol{x}_k}\right) \approx \frac{1}{2}\left(\frac{\partial \boldsymbol{u}_i}{\partial \boldsymbol{x}_k} + \frac{\partial \boldsymbol{u}_k}{\partial \boldsymbol{x}_i}\right) . \tag{1.1}$$

The strain tensor is symmetric, and so can be diagonalized at any given point with an appropriate choice of coordinate axes. In the case of small deformations, wherein the change in distance between two points after deformation is much smaller than the distance itself, the strain tensor can be approximated as the expression seen to the far right-hand side of (1.1).

When a body undergoes a deformation, it ceases to be in mechanical equilibrium and experiences internal forces, which work to return the body to equilibrium. These internal forces are referred to as *internal stresses* and occur only in the case that the body is deformed. The internal stresses inside a tissue are generated by molecular and cellular forces from the cells, though the influence of these forces extend only to an order of distance within its neighboring cells, whereas

elasticity theory is concerned with distances much larger than the scale of individual cells. The *stress tensor*, σ_{ik}, contains the information about the internal stress of a body at a given point, describing the *i*-th component of the force on unit area perpendicular to the x_k-axis, which can be defined with respect to the strain tensor via

$$\sigma_{ik} = \left(\frac{\partial F}{\partial u_{ik}}\right)_T , \tag{1.2}$$

where *F* is the free energy of the body per unit volume and *T* assumes a constant temperature.

With this, one can obtain an expression for the free energy of a body as a function of the strain tensor, by assuming small deformations and expanding in powers of u_{ik}. In an isotropic body at constant temperature, expanding the free energy out to second order gives

$$F = F_0 + \frac{1}{2}\lambda {u_{ll}}^2 + \mu {u_{ik}}^2 , \tag{1.3}$$

where λ and μ are called *Lamé coefficients,* both with units of force per unit volume. μ is also referred to as the *shear modulus,* measuring a material's resistance to forces imposed on its body in opposite directions. We also have the *bulk modulus,* defined in two dimensions simply as $\kappa = \lambda + \mu$, which measures a material's resistance to compression and will later be used to rewrite (1.3) in terms of κ and μ.

1.3 Hyperuniformity

Cellular arrangement is an important aspect of understanding tissue behavior in morphogenesis due to the spatial structure of cells influencing its mechanics. Studying the arrangement of biological tissue is inherently more complicated than the study of, say, crystals, since it is a disordered material lacking the symmetries or periodicity usually at one's disposal to simplify matters. Despite the limited toolset available, a common measurement used to characterize the spatial structure of disordered media is through density fluctuations [31, 32]. A recurring observation throughout this thesis will be the suppression of density fluctuations found in simulations from the vertex model, referring to the tendency of cells in a tissue to coordinate themselves uniformly in space. Disordered systems which exhibit suppression of density fluctuations at large length scales are said to be *hyperuniform,* which share this behavior with crystals, and yet also appear to be statistically isotropic like a liquid or glass. Hyperuniformity in

disordered media has gained more attention in recent years in the context of biophysics, and different strategies have been developed to better quantify it [20, 33, 34, 35, 36].

For our purposes, cell centroids are represented by points restricted to a plane in two dimensions. For a system of *n* particles, the number of points counted within a single, circular measurement window of radius *R* with center position $\boldsymbol{r}_c$ can be written as a function of the radius length,

$$N(R) = \sum_{i}^{n} \Theta(R - \|\boldsymbol{r}_i - \boldsymbol{r}_c\|) \ , \tag{1.4}$$

where $\boldsymbol{r}_i$ is the position of the centroid of a cell and $\Theta(\mathrm{x})$ is the Heaviside function. Density fluctuations for this distribution of points are characterized by calculating the variance of the number of points within an ensemble of circular measurement windows placed randomly throughout the packing,

$$\langle \delta^2 N \rangle = \langle N(R)^2 \rangle - \langle N(R) \rangle^2 \ , \tag{1.5}$$

where $\langle \dots \rangle$ represents an ensemble average. In two-dimensional space, density fluctuations of a collection of independent, uniformly distributed points scales like the volume of the measurement window, $\langle \delta^2 N \rangle \sim R^2$. A crystalline or otherwise regular distribution, however, scales like the surface area, $\langle \delta^2 N \rangle \sim R$. Disordered hyperuniformity, then, is thus described as density fluctuations which scale somewhere between these two, $\langle \delta^2 N \rangle \sim R^{\epsilon}$, where $1 \leq \epsilon < 2$, as $R \to \infty$, capturing the suppression of density fluctuations at long-length scales [33].

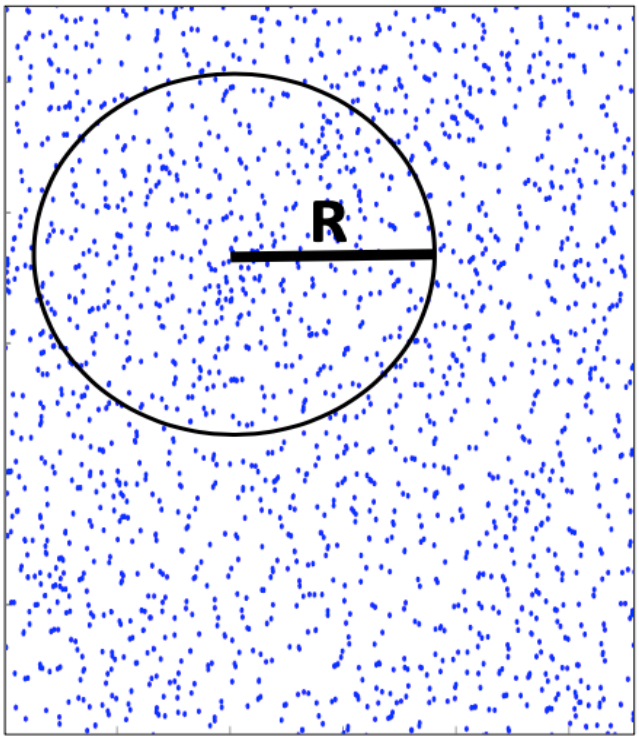

FIG 1.3: Example of randomly distributed points with a single measurement window of radius *R*. An ensemble of measuring windows such as this with varying radius lengths are placed throughout the plane to count the number of points contained within each. Density fluctuations of the packing are then characterized using eq. (1.5).

A priori, one expects an epithelial sheet with linear elastic properties to exhibit $\langle \delta^2 N \rangle$ that scales as the volume of the measurement window. This expectation can be derived using a result borrowed from a recent publication from Damavandi and Lubensky, which proposes a theoretical framework describing the growth of elastic tissues with stochastic noise and mechanical feedback [37]. In the paper, tissue growth is represented using a symmetric second rank tensor composed of average growth component, $\bar{G}$, and a component describing noisy fluctuations around the average, $\tilde{G}$. With a material density defined similarly with a uniform and fluctuating component, $\rho(\boldsymbol{r}) = \rho_0 + \delta\rho(\boldsymbol{r})$, density fluctuations in this model assuming an infinite tissue is related to growth by

$$\delta\rho = \rho_0 \frac{\mu}{\lambda + 2\mu} \left(\frac{\widetilde{G_{ll}} - 2\widetilde{G_{\parallel}}}{\bar{G}} \right) \quad . \tag{1.6}$$

This expression is written in Fourier-space with $\widetilde{G_{ll}}$ as the trace of the fluctuating growth tensor, and $\widetilde{G_{\parallel}}$ as the traceless part of $\tilde{G}$ parallel to the frequency vector.

To estimate the amount of material or cells within a given measurement window of volume Ω from this framework, one can integrate over the volume of a circular measuring window of radius R to find

$$N_{\Omega} = \int_{\Omega} d^3\boldsymbol{r}\, \rho(\boldsymbol{r}) = \rho_0 \pi R^2 + \int_{\Omega} d^3\boldsymbol{r}\, \delta\rho(\boldsymbol{r})\,. \tag{1.7}$$

Since variance is defined in terms of a random variable subtracted from its mean, the first term on the right-hand side is dropped and we are left with the desired expression,

$$\langle \delta^2 N \rangle = \int_{\Omega} d^3\boldsymbol{r} \int_{\Omega} d^3\boldsymbol{r}'\, \langle \delta\rho(\boldsymbol{r})\delta\rho(\boldsymbol{r}') \rangle\,. \tag{1.8}$$

If the noise in $\tilde{G}$ is delta correlated in space, then we have that $\langle \widetilde{G_{ll}}(\boldsymbol{r})\widetilde{G_{ll}}(\boldsymbol{r}') \rangle \sim \delta(\boldsymbol{r}-\boldsymbol{r}')$, $\langle \widetilde{G_{\parallel}}(\boldsymbol{r})\widetilde{G_{\parallel}}(\boldsymbol{r}') \rangle \sim \delta(\boldsymbol{r}-\boldsymbol{r}')$, and $\langle \widetilde{G_{ll}}(\boldsymbol{r})\widetilde{G_{\parallel}}(\boldsymbol{r}') \rangle = 0$, such that $\langle \delta\rho(\boldsymbol{r})\delta\rho(\boldsymbol{r}') \rangle \sim \delta(\boldsymbol{r}-\boldsymbol{r}')$ from equation (1.6). This implies that the integral of equation (1.8) is proportional to the volume of the measurement window, in this case, $\langle \delta^2 N \rangle \sim R^2$.

Thus, there is reason to suspect that a large sheet of epithelial cells should exhibit a variance of the number of cells within a measuring window to scale like its volume, and so appear random in its arrangement.

1.4 Format

This thesis is composed of three chapters. Chapter II will discuss further specifics of the vertex model and how simulations of epithelia are constructed. Results will be shown of tissue simulations that exhibit anomalous hyperuniform behavior, as well as document the challenges and attempts made to understand its occurrence. This will involve developing a practice to measure density fluctuations from simulation data and comparing it to the bulk and shear properties of the tissue. The method in which these quantities are extracted is also explained. In Chapter III, the vertex model is used to test the predictions made by the publication mentioned in the previous section, whereby a handful of cells are randomly marked as clones and observed as the tissue grows to examine the statistics of their size. We find agreement with some predictions made by the model, though evidence of hyperuniformity in its results imply that our simulations may be

displaying unexpected nonlinear behavior that creates disagreement between the two models. Finally, in Chapter IV, attention is given to our most recent efforts made to identify and characterize hyperuniformity in disordered elastic media. We call attention to the development of a new model which seeks to ensure hyperuniformity is a result of nonlinear elastic deformations, and not from flow or plastic deformations. Afterwards, we briefly discuss potential directions for the project to be taken in the future.

CHAPTER II

Observed Hyperuniformity in Vertex Model Simulations

The process by which epithelial cells can arrange themselves into cohesive biological structures of profound complexity and importance is as interesting as it is intimidating. Attempting to apply the tools available through the language of biophysics and recent innovations of computation open the doors to describing how these phenomena occur, but they are not without their challenges. Early in our efforts to study the spatial structure of tissues in the vertex model, we observed that cells seemed to be demonstrating hyperuniform density fluctuations. Throughout each chapter of this thesis hyperuniformity plays a role, and it quickly became apparent that understanding its cause would be a priority. This chapter, then, will detail the vertex model's first encounter with hyperuniformity and the progress made in identifying the mechanisms that cause it.

2.1 Vertex Model

Here will be provided an elaboration on the vertex model used to simulate epithelial tissue further than what was mentioned in Chapter I. The vertex model seeks to evaluate the mechanics of epithelium using *cells, edges,* and *vertices,* a diagram of which is illustrated in fig. 1.1. Edges are straight line approximations of the adherens junctions described in Section 1.1, and capture the contractile behavior found along cell borders. Vertices are the points at which three or more edges meet and define the motion and degrees of freedom allowing the model to evolve into its final morphology. The forces felt by each vertex are generated from both edges and cells, where mechanical equilibrium is realized via a balance of the tensions produced by these edges with internal pressures assigned to each cell [24]. These forces are derived from an effective energy functional dependent on vertex positions, given by

$$U = \sum_i \Gamma_i l_i + \frac{K}{2} \sum_\alpha (A_\alpha - A_{0\alpha})^2 \ . \tag{2.1}$$

The first sum indexes over all edges, where edge *i* has assigned tension Γ_i and length l_i. This term captures the effects of both cell-cell adhesion and actomyosin contractility of cellular junctions. The second sum indexes over all cells in the tissue, where each cell α has an actual area A_α and an assigned preferred area $A_{0\alpha}$. This term describes the energy cost associated with deforming a cell from its preferred area, and the parameter *K* modulates the strength of this energy cost.

The final shape of the tissue is then determined by reaching some local minimum of this effective energy. Since the vertex model describes cells evolving on relatively slow timescales in a viscous medium, inertial effects are negligible, and the evolution of the vertex positions towards this energy minimum is assumed to obey relaxational dynamics [21]. The force on each vertex used to reach this minimum can be found by taking the derivative of the energy with respect to vertex position. Since a small movement of one vertex only changes the lengths and areas of its neighboring edges and cells, respectively, the sum over all edges *i* and all cells α becomes a sum over all neighboring edges $[i]$ and all neighboring cells $[\alpha]$ to that vertex. The force on a vertex at position $\boldsymbol{r}_0$ imparted by its surrounding edges and cells is then given by

$$F_{\boldsymbol{r}_0} = -\frac{\partial U}{d\boldsymbol{r}_0} = \frac{K}{2}\sum_{[\alpha]}(A_{0\alpha} - A_\alpha)\,[\hat{z} \times (\boldsymbol{l}_{\alpha 2} - \boldsymbol{l}_{\alpha 1})] + \sum_{[i]} \Gamma_i \widehat{\boldsymbol{l}_i}\ . \tag{2.2}$$

Here $\boldsymbol{l}_{\alpha 1}$ and $\boldsymbol{l}_{\alpha 2}$ are vectors with length of the two edges neighboring both the vertex with position $\boldsymbol{r}_0$ and cell α, and $\widehat{\boldsymbol{l}_i}$ is a unit vector of edge $[i]$ pointing away from $\boldsymbol{r}_0$. Motion of the vertices is determined by assuming that vertices undergo a drag force proportional to their velocity, such that the positions of a vertex obey the equation of motion

$$\frac{d\boldsymbol{r}_0}{dt} = \frac{\boldsymbol{F}_{\boldsymbol{r}_0}}{\mu_t}\ , \tag{2.3}$$

where μ_t is a drag constant that helps set the timescale of the simulations. Although Γ_i can be assigned unique values for each edge, we restrict ourselves to an *equal tension model,* such that $\Gamma_i = \Gamma$, as a general case where edge tensions are slower to respond to stress. Likewise, we assign a consistent preferred area to each cell, $A_0 = \frac{L_X L_Y}{n}$, where *n* is the number of cells in the packing, which is confined to a box of size L_X by L_Y with periodic boundary conditions.

Our implementation of the vertex model uses a C++ framework capable of receiving a full description of a tissue as an input, including any relevant parameters and all information needed to describe vertex positions and edges connecting them [16]. At the end of a simulation, an output file may be created that contains this same description of the tissue, so it may be used as its own input if desired, along with any other data that one wishes to extract. The equations of motion are integrated using a variable step-size fourth order Runge-Kutta scheme. This choice of integrator was chosen rather than, say, a fixed Euler integrator, because there are often periods in the evolution of a tissue involving topological changes that require small time steps to minimize errors, but these are often followed by long periods during which the tissue is relaxing towards its equilibrium configuration and there is very little motion, and so larger integration steps can be used to reduce computation time. These time steps of variable lengths used by the integrator are distinct from *time intervals*, which are larger units of time of fixed length within the model, when output data is written or other tasks like mitosis are performed. T1 transitions can happen at any given time step to allow cells to rearrange themselves whenever needed, though mitosis and apoptosis can only be initiated at full time intervals.

2.2 Simulation Conditions and Observed Hyperuniformity

As noted above, the simulations use periodic boundary conditions such that the cells evolve inside a box of length L_X in the x-direction and length L_Y in the y-direction (with $L_X = L_Y$ in most cases), so the cells in the simulation can topologically be thought as living on the surface of a torus. The use of periodic boundary conditions is useful, due to its ability to approximate an infinite system with a finite system of cells. Applying concepts from elasticity theory often assume that a material exists along an infinite sheet [29], so this is particularly convenient for comparison to theoretical models, as is done in Chapter III. If cells are added to the tissue via mitosis or removed via apoptosis at any time interval, the size of the box is preserved, and the tissue itself is rescaled without the mechanics of the vertices being disrupted, where the preferred area of the cells change according to the number of cells in the packing.

Initial conditions of the packing are prepared using a MATLAB script specifying any parameter choices and starting configuration of the cells within the simulation. For the results featured in this thesis, initial configurations were generated by creating a Voronoi tessellation.

This involves placing down points onto a plane with a Poisson distribution and partitioning the plane into cells such that the space in each cell is closer to its corresponding point than any other point in the plane. This ensures that the cells begin with an approximately random arrangement so they can relax to some unique configuration as it reaches a local energy minimum.

MATLAB was used for both visualization of the tissue's evolution through time and for the analysis of any data extracted from the simulations. At each time interval, data is recorded to an output file that contains the information necessary to completely reconstruct the tissue. This can be used to produce movies that show the evolution of the packing in time, which is essential to confirm that the tissue is behaving physically and demonstrating the properties one expects. To characterize density fluctuations of the tissue, a MATLAB script was written that allows one to plot $\langle \delta^2 N \rangle$ as a function of R for the configuration of a simulation at a given time interval. The function stores the position of the centroid of each cell from the output of a simulation so the number of cells can be counted that lie within a circular measurement window. An array of radii is chosen ranging from a minimum radius corresponding to the mean edge length of all edges in the packing to a maximum radius corresponding to $L_X/4$. More radius measurements mean more data points, and thus a more detailed picture of the density fluctuations at different length scales of the tissue. The number of measurement windows sampled for each radius measurement affects how closely each data point resembles the true value for $\langle \delta^2 N \rangle$ at a given length scale. Each of these measurement windows are placed randomly inside the box, respecting periodic boundary conditions, and count the number of cell centroids within them, as in (1.4). For each distinct radius measurement, the variance of the number of cells counted for each window in the ensemble is calculated.

Figure 2.1 (a) shows a log-log plot of $\langle \delta^2 N \rangle$ normalized by R^2 as a function of R. To produce these simulation results and others later in this chapter, an initially random Voronoi tessellation of 10^4 cells was relaxed until a configuration was produced having reached mechanical equilibrium. These plots were created by averaging the data from 10 different simulations, each with uniquely seeded initial tessellations. Values for Γ and K can be found in Table 2.1, chosen historically to align with experimental data from *Drosophila* wing discs [38]. Assuming the ansatz that the plots should follow a power law $\frac{\langle \delta^2 N \rangle}{R^2} \sim aR^m$, we can perform a linear fit to estimate the exponent and characterize the density fluctuations of the epithelium. Here an exponent of $m = -1$

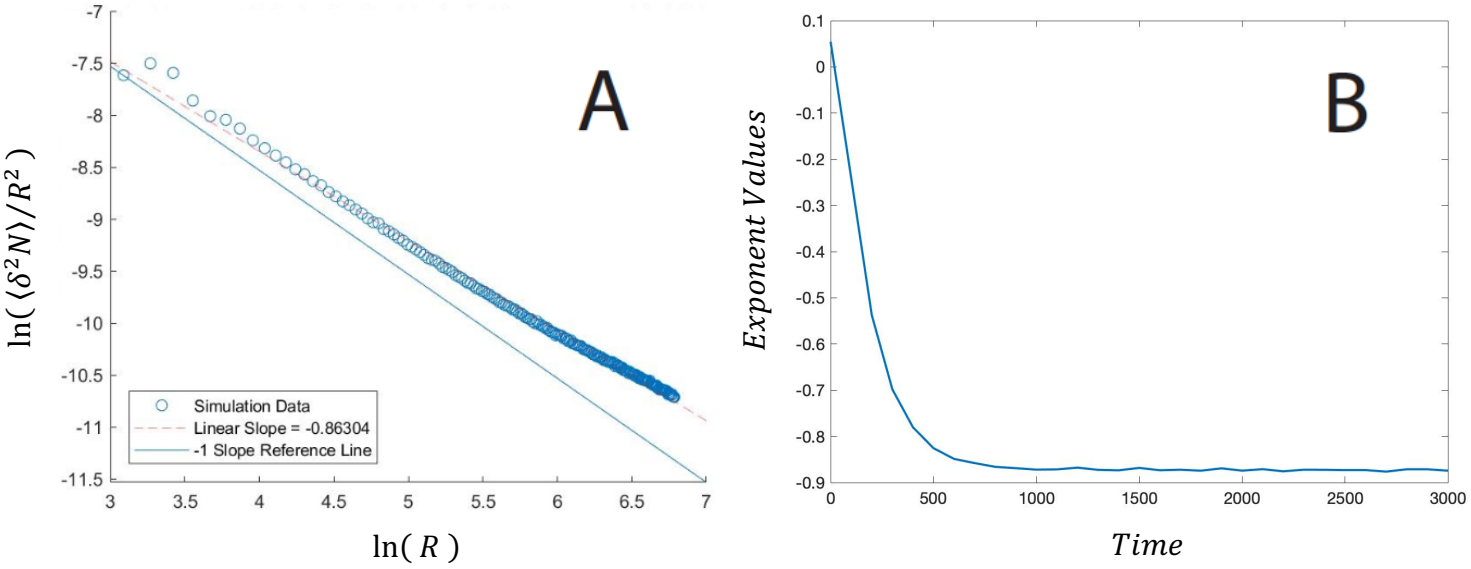

FIG 2.1: **A** Log-log plot of $\langle\delta^2 N\rangle/R^2$ as a function of R for the final relaxed configuration of a system of 10^4 cells, averaged over 10 different simulations. The blue line is a reference for the slope of a curve demonstrating perfect hyperuniformity, whereas a horizontal slope would represent that of a random distribution of cells. The red dashed line is a linear fit that estimates the exponent of the power law behavior, showing that the density fluctuations of the tissue are highly suppressed. **B** Plot of the extracted exponent values for density fluctuations at different time intervals. The data starts near a value of 0 from the initially random Voronoi tessellation, and quickly decreases towards hyperuniformity as the packing relaxes.

corresponds to a packing exhibiting perfect hyperuniformity, whereas $m = 0$ to that of an uncorrelated, uniform distribution of cells.

The data implies a clear suppression of density fluctuations at long length scales. Small perturbations can be seen at the onset of the curve due to finite size effects from measuring windows being close to the characteristic cell size. By extracting the exponent at different time intervals throughout the evolution of the packings, we can also create plots illustrating how this quantity changes with time, shown in fig. 2.1 (b). We will see that the data does not always conform exactly to a power law due to finite size effects as measurement windows approach the characteristic cell size or the size of the box, especially for early time intervals in the simulations. For this reason, the fits for the exponents do not always reflect that of a perfect power law, and so fig. 2.1 (b) should serve only as a rough indication for how the density fluctuation curves evolve in time.

2.3 Elastic Properties of the Simulated Tissue

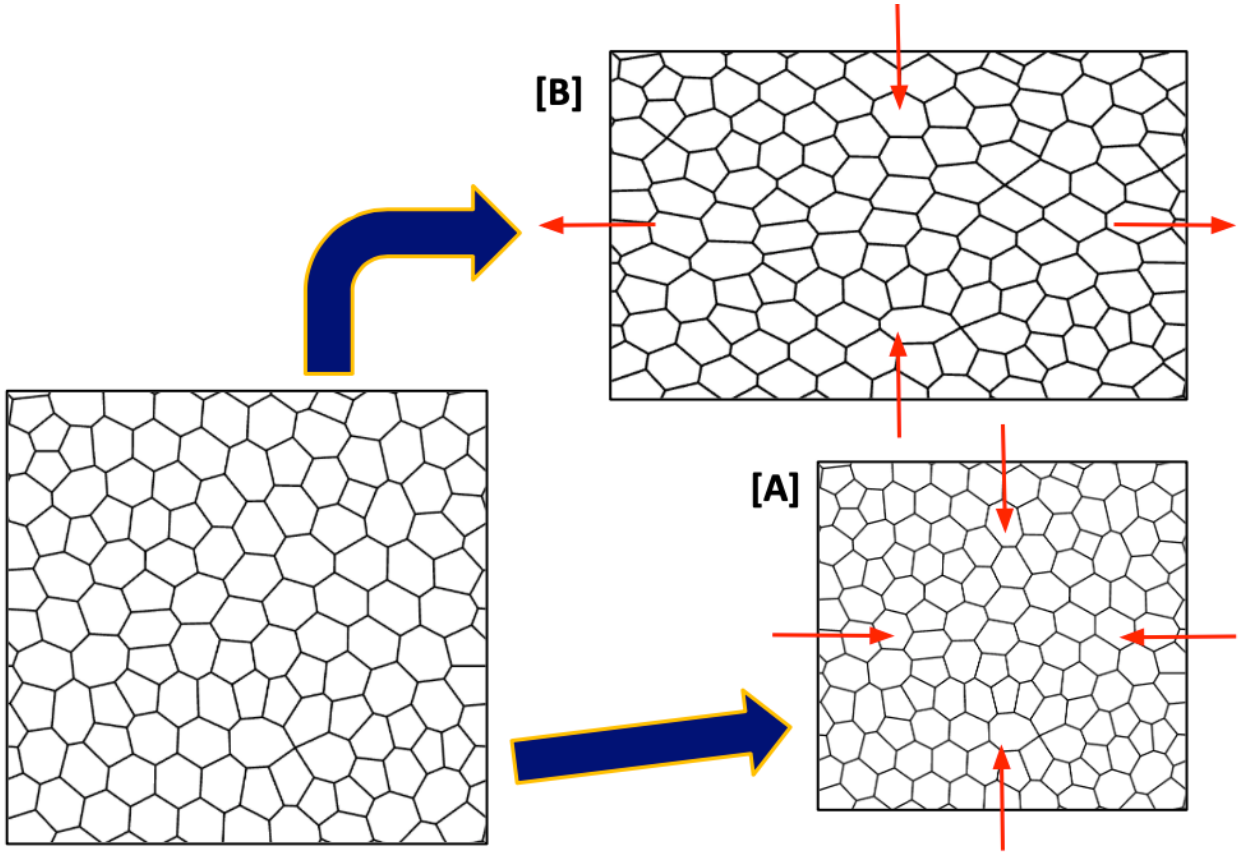

FIG 2.2: Cartoon of a small packing of cells from the vertex model simulations before and after a deformation is applied (exaggerated here for visualization purposes). **A** Application of a hydrostatic compression on the tissue. **B** Application of a squeeze deformation on the tissue, preserving the total area of the box.

Due to the unexpected result of identifying such pronounced suppression of density fluctuations in these packings, one hypothesis is that if statistics were collected for considerably larger tissues, and so extend the data for $\langle \delta^2 N \rangle$ to even further length scales, the system would experience a crossover in behavior, transitioning from the displayed hyperuniformity to a more horizontal curve, as predicted by linear elasticity theory [37]. As can be seen in fig. 2.1 (a), there is a slight increase in the slope of the data that may suggest the presence of a continuous crossover beginning to occur. Recent papers have made observations of hyperuniformity in disordered

packings using similar computational models, and by modulating parameters controlling the dynamics of their simulations, found evidence of a crossover from hyperuniform to Poisson behavior at long length scales within the solid phase, with the scale at which the crossover occurs diverging as the fluid phase is approached [20,33]. In the fluid phase, however, hyperuniformity was shown to be maintained without a crossover. The vertex model we work with does not have a fluid phase, since our energy functional uses a linear tension, preventing the packing from freely moving between different equilibrium configurations with no cost in energy, which is characteristic of a fluid.

This implies that the choice in parameters of our model may be causing the tissue to behave *similar* to a fluid, where the cells are able to rearrange themselves uniformly with few barriers. A fluid, by definition, has zero shear modulus, so it is reasonable to suspect that the tissue behaving fluid-like may correspond to it possessing a shear modulus that is significantly smaller than its bulk modulus. While our model is not capable of behaving like a true fluid, it can exhibit nonlinear elastic behavior with a soft shear modulus, where cells move about with very little energy cost. This suggests a relationship between the length scale at which hyperuniformity breaks in tissue simulations and the bulk and shear moduli, which are physical quantities. We then want to find a way to modulate these elastic properties of the tissue by changing the parameters of the simulation. To do this, it is necessary to develop a method which determines the bulk and shear moduli directly from simulation data. This will be done by deforming a relaxed tissue packing via imposing a hydrostatic compression to isolate the bulk modulus, or via a pure shear to isolate the shear modulus. Using (1.3), we can deform the packings for different scalar values of strain and compare them with the total energy of the system, then conduct the appropriate fits to recover estimates for both moduli. It is convenient to decompose (1.3) to separate it into pure shear and hydrostatic compression components and omit the free energy of the undeformed body,

$$F = \mu(u_{ik} - \frac{1}{2}\delta_{ik}u_{ll})^2 + \frac{1}{2}\kappa {u_{ll}}^2 \ . \tag{2.4}$$

To estimate the bulk modulus, a hydrostatic compression or expansion is imposed on the tissue after it has reached a relaxed state. The dimensions of the box size then rescale to ${L'}_X = \alpha L_X$ and ${L'}_Y = \alpha L_Y$, with α as a small scaling factor taking values close to 1. This type of deformation has zero non-diagonal components for the strain tensor of the material, so the first term of (2.4) is dropped and the free energy can be found by integrating over the volume of the box,

$$E^{(\kappa)} = \frac{1}{2} L_X L_Y \kappa {u_{ll}}^2 \,, \tag{2.5}$$

where the trace of the strain tensor for this deformation can be derived from (1.1) as $u_{ll} = 2(\alpha - 1)$. This expression allows one to deform a tissue over many values of α to make plots comparing the total energy of the tissue at different levels of strain and make a fit to extract an estimate of κ, seen in fig. 2.3 (a).

For the shear modulus, a pure shear is imposed by expanding the packings in one direction and compressing in the other direction in such a way that preserves the total area of the box, which we will call a *squeeze* deformation. The dimensions of the box rescale to ${L'}_X = \alpha L_X$ and ${L'}_Y = \frac{1}{\alpha} L_Y$. Contrary to the previous case, this drops the κ dependency of (2.4) and the free energy is found similarly by integrating over the volume of the box,

$$E^{(\mu)} = L_X L_Y \mu {u_{ik}}^2 \,, \tag{2.6}$$

where the sums of the squared components of the strain tensor for this deformation can be derived to be $u_{ik}^2 = (\alpha - 1)^2 + \left(\frac{1}{\alpha} - 1\right)^2$. We can use this similarly to extract an estimate for μ, as shown in fig. 2.3 (b).

K	Γ	κ	μ	μ/κ
0.003264	17.4859	3.8383	0.2185	0.0569
0.003264	8.7430	3.9595	0.1089	0.0275
0.006528	17.4859	7.9199	0.2229	0.0281
0.001632	17.4859	1.7925	0.2172	0.1211
0.003264	34.9718	3.5858	0.4404	0.1228

Table 2.1: Displayed in each row are the parameter schemes used to produce the $\langle \delta^2 N \rangle$ curves in fig. 2.4 (a). The first row shows the original set of parameters used and corresponding bulk and shear moduli. The remaining parameter schemes are arranged in order of increasing μ/κ.

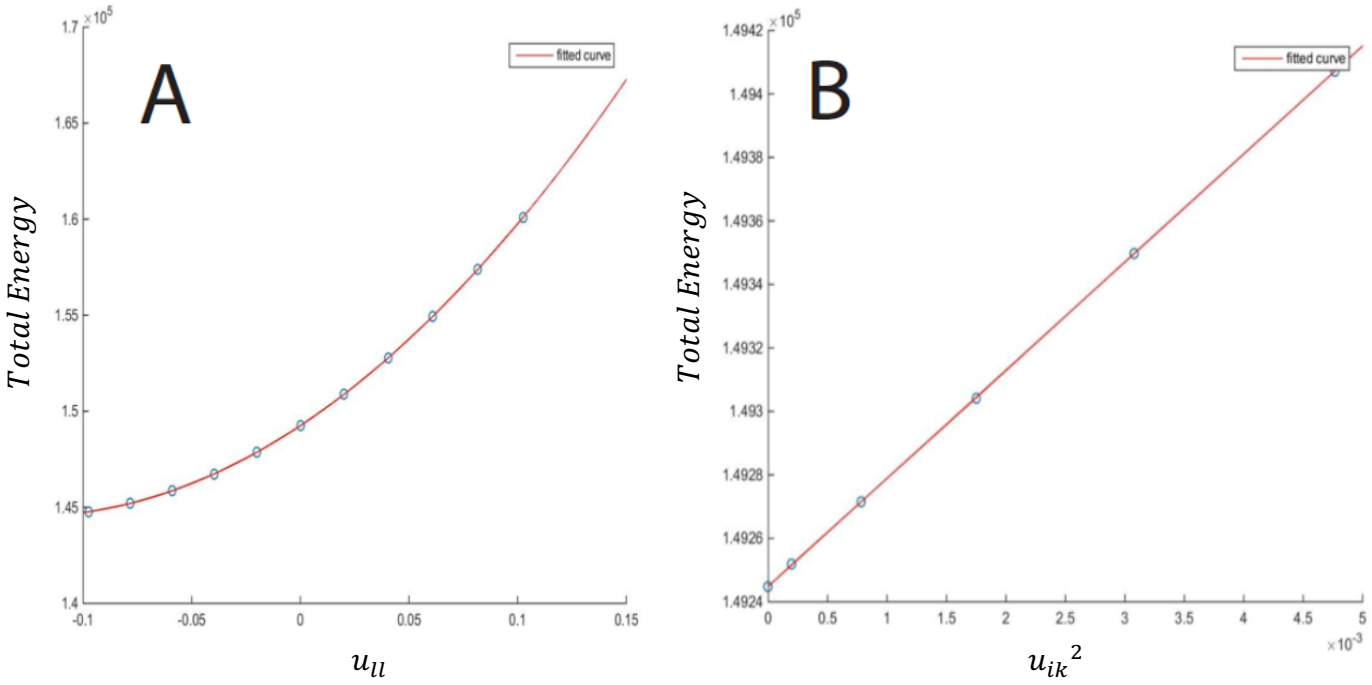

FIG 2.3: **A** Plot of the total free energy of a tissue simulation after imposing hydrostatic compression or expansion for different values of u_{ll}. The red curve fits the data to the form of (2.5) to estimate the bulk modulus of the system. The minimum for this plot occurs for even lower values of strain, since further compression would be needed for the increase in energy due to cells shrinking to overtake that of the energy decrease from edge tensions. **B** Plot of the total free energy of a tissue simulation after imposing a squeeze deformation for different values of ${u_{ik}}^2$. We plot energy in terms of ${u_{ik}}^2$ to acquire a linear fit for (2.6) to estimate the shear modulus of the system, for convenience.

2.4 Results for Varied μ, κ

The moduli were found by fitting data taken from an average of 15 simulations with unique initial configurations, and from these fits estimated that $\kappa = 3.8380$ and $\mu = 0.2182$ (with units of force per unit volume) using the original parameters for Γ and *K*. This suggests that the shear modulus of these tissue simulations is, in fact, much lower than the bulk modulus, supporting the idea that a small ratio between the shear and bulk moduli are contributing to the displayed suppression of density fluctuations. To further this claim, the moduli from simulations using different choices in parameters were taken, the values of which can be found in Table 2.1. Changes in energy due to compressions or expansions are dominated by the deformation of cell areas in (2.1), so the bulk modulus of the tissue is expected to scale proportionally to our choice in *K*.

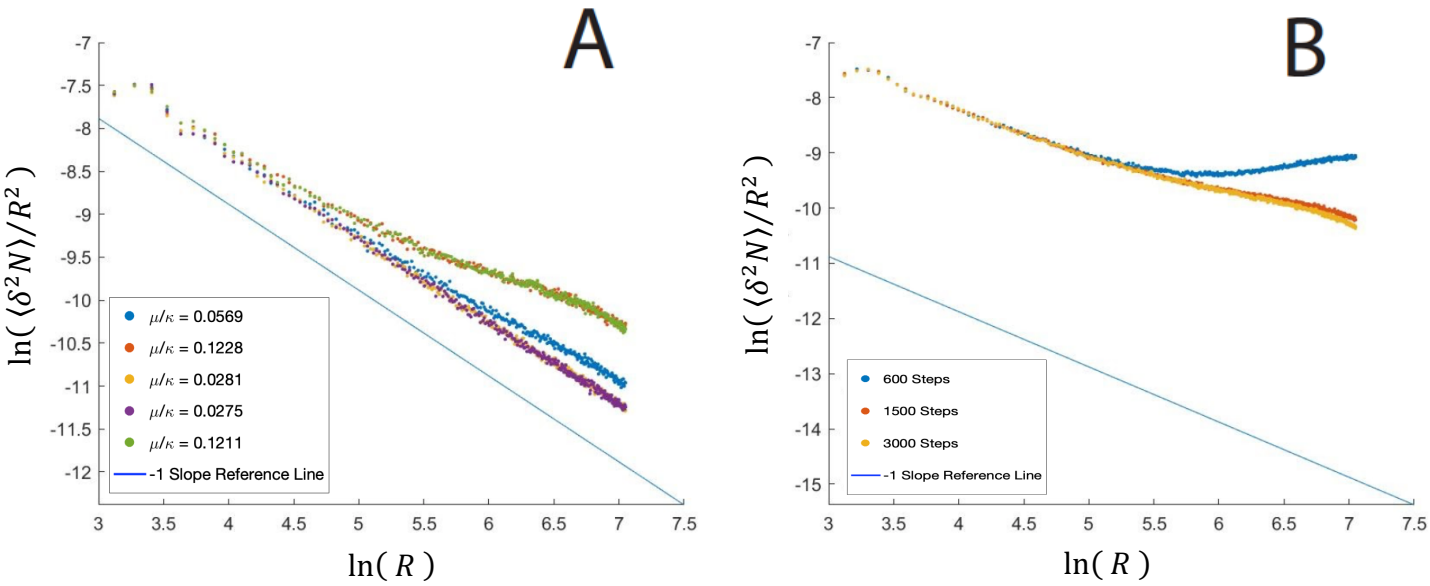

FIG 2.4: Log-log plots of $\langle\delta^2 N\rangle/R^2$ as a function of R for the final relaxed configuration of a system of 10^4 cells. The blue lines are a reference for the slope of a curve possessing the slope of a curve demonstrating hyperuniformity, whereas a zero slope would represent that of a random distribution. **A** Shows density fluctuation curves for different bulk and shear modulus schemes. We see that decreasing Γ or increasing K (decreasing the ratio of μ/κ) by a factor of 2 produces greater suppression of density fluctuations. In contrast, increasing Γ or decreasing K (increasing the ratio of μ/κ) by a factor of two diminishes this suppression. **B** We choose an arbitrary parameter ($\mu/\kappa = 0.1211$ in this case) to demonstrate the behavior of these curves before the simulations have properly relaxed. Failing to reach a minimized energy configuration can hint towards a crossover that is not representative of the equilibrated state of the tissue.

Likewise, since applying a pure shear to the packings largely maintains the initial area of each cell, the change in energy should be dominated by edge tensions, hence the shear modulus scaling proportionally to Γ. Furthermore, inversely scaling the parameters of the simulations (i.e., doubling Γ and halving K) should lead to an identical ratio of bulk to shear, $\frac{\mu}{\kappa}$, and so should demonstrate similar cell distributions. To show this, four different sets of parameters were chosen to simulate and compare fluctuations. In each case, either Γ or K are doubled or halved from its original value.

The $\langle\delta^2 N\rangle$ data corresponding with K being doubled and Γ being halved demonstrate fluctuations suppressed even more than with the original parameters as expected, aligning almost exactly with the reference line indicating a perfectly hyperuniform distribution. The opposite cases

when Γ is doubled and K is halved appear to be less uniform than the other sets of data. We even see a sign of an increase in the slopes, suggestive of a continuous crossover, although the slope of these two curves seem to decrease at longer length scales. This decrease at large R is likely not truly representative of the architecture of the cells, but instead a result of finite size effects as measuring windows become comparable to the size of the box, causing correlations in the statistics collected by the windows which systematically decrease the variance measurements collected. Despite this discrepancy near the tail end of the data, the results verify the claim that density fluctuations are suppressed for decreased ratios of $\frac{\mu}{\kappa}$, while becoming less suppressed for increased ratios of $\frac{\mu}{\kappa}$.

2.5 Conclusion

We have thus found that the vertex model exhibits hyperuniform density fluctuations, and that the extent of these fluctuations depends on the shear to bulk ratio of the tissue. The methods and conclusions presented represent meaningful strides towards relating the anomalous hyperuniformity seen in simulations of epithelial tissue with physical quantities that, if developed further, could be used as a theoretical framework to be tested against experimental findings. Although the initial application of the described methods used to compare the density fluctuations of tissues against different ratios of $\frac{\mu}{\kappa}$ was promising, a few challenges quickly made themselves apparent that would intervene with our ability to produce the results needed to continue using the same model.

First, as was hinted to by the decrease of $\langle \delta^2 N \rangle$ for large R, there is a need to generate even larger numbers of cells to observe fluctuations at larger length scales without the intervention of finite size effects. To be confident in the existence of a continuous crossover that may appear over long distances, statistics should be collected from a tissue of a size far exceeding what was shown above. This is necessary to see the full crossover, which means reaching length scales long enough such that the $\langle \delta^2 N \rangle$ curves become clearly horizontal. However, adding cells has a significant impact on the time required to reach equilibrium, the computational efforts of which would outpace the time constraints for this project. In addition, a broader range of parameter choices increasing the value of $\frac{\mu}{\kappa}$ would be needed to develop a strong relationship between this ratio and the

occurrence of hyperuniformity, though this is hampered by the slowing of dynamics as one increases Γ or decreases *K*. One can define a mechanical timescale for the vertex model dependent on these parameters, given by $\tau = \frac{\mu_t l_0}{\Gamma}$ or $\tau = \frac{\mu_t l_0}{K {l_0}^3}$, where l_0 represent the average length of an edge [38]. To change Γ or *K* in a way that increases $\frac{\mu}{\kappa}$ causes a decrease in the time scale of the dynamics, such that the mechanical timestep for the simulations must also necessarily decrease in response. This causes the simulations to slow significantly, and, combined with the need for larger tissues discussed prior, can make the relaxation time required for tissues at high values of $\frac{\mu}{\kappa}$ infeasible. To illustrate the effects not relaxing a packing until proper equilibrium is reached can have on data, fig. 2.4 (b) is provided to show how the $\langle \delta^2 N \rangle$ curve evolves at different intervals during the simulation. It is evident that not allowing the tissue enough time to relax can produce results that may imply a crossover event that is not truly emblematic of the fully relaxed configuration.

Additionally, increasing the ratio of the moduli involves a modulation of the parameters that puts a heavy emphasis on the contractile forces from edge tension, and diminishing those from area deformations. This tends to disrupt the balance between these forces for more extreme parameter schemes and induces widespread topological changes in the form of apoptosis and T1 transitions on account of edges experiencing less resistance from contracting. Not only does this often lead to an unacceptable reduction in the number of cells in the packing or crashing altogether, but it represents a systematic breakdown of mechanics that disrupts the relaxation process and thus yields behavior that is not comparable with other results.

Although these initial findings were promising, the barriers presented by the vertex model indicated that a different model must be employed pursue them further. The efforts made toward developing such a model can be found in the contents on Chapter IV.

CHAPTER III

Clone Statistics

The study of clones to track growth and development of biological tissues is a useful method for many areas within cell biology [39,40]. A *clone* is a group of cells that are genetically identical to one another, marked in some way allowing the progeny of these cells to inherit this marking and be distinguished from cells surrounding them. This can be used, for example, in tracking the lineage of cells of embryonic organs, wherein individual cells are marked with a fluorescent reporter gene which is then used to observe clone sizes and composition throughout development. The use of clones can also commonly be found in the study of stem cell fate and tumor growth [41,42,43]. Here, clones are utilized as a means of understanding stochasticity in elastic tissues. There is noise inherent to the growth of any biological system that can play a significant role in development, but stochastic growth of tissues is, as of yet, a largely unexplored subject.

This chapter will focus on testing a theoretical model of growth in elastic tissues proposed by Damavandi and Lubensky, a paper published by our group from 2019 [37]. The model involves a flat, two-dimensional epithelium treated as an elastic continuum. It assumes an infinite tissue growing exponentially on average, where random fluctuations can induce linear elastic deformations and thus local mechanical stress. A linear feedback of the stress tensor is implemented on the local growth rate, which serves to relax stress where it occurs. The paper looks at the dynamics of marked clones genetically identical to the surrounding tissue (called *neutral* clones) assuming both isotropic and anisotropic growth. For the case of anisotropic growth, it is predicted that the variance of clone sizes scales like the average area squared and that the area of large clones is just as variable as that for small clones. Verifying these predictions is the subject of this chapter and will involve comparing properties of continuous medium to those collected from the discretized cell equivalent of the vertex model. To acquire these results, clone tracking features were implemented into the simulations, as well as a pressure dependent feedback system on division rate. Before discussing these implementations, a brief overview will be given to the details of the continuum model needed to derive the equations used for comparison with simulation data.

3.1 Continuum Model Overview

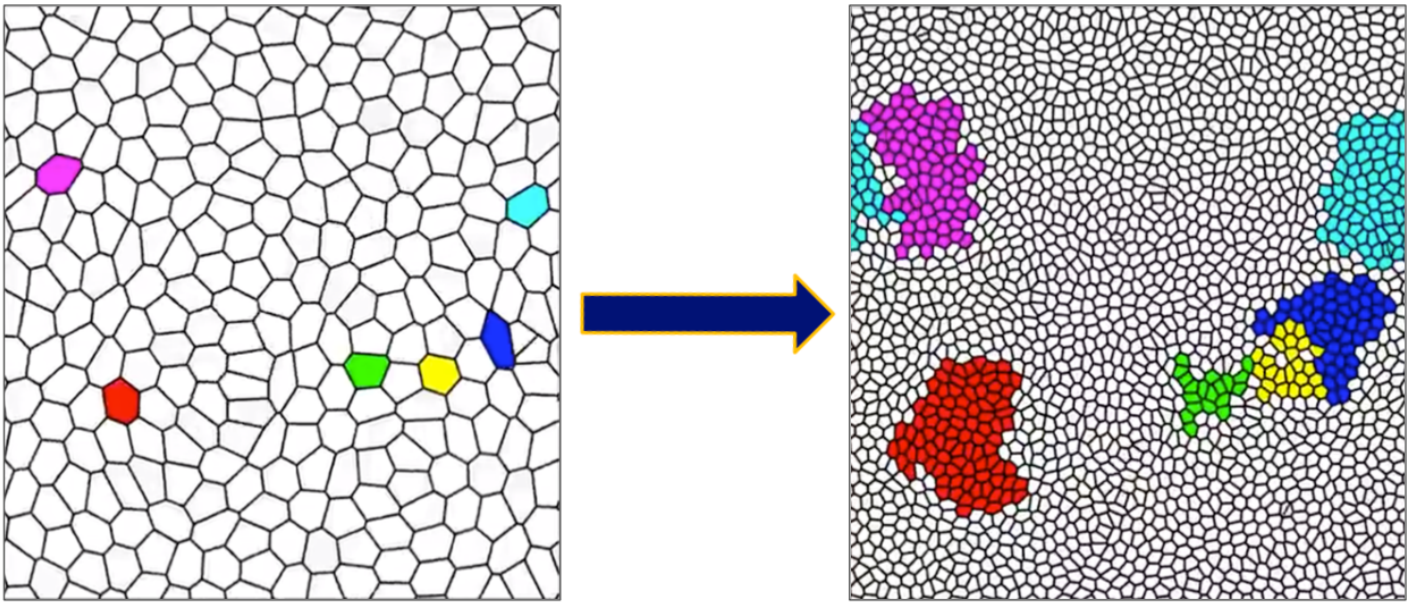

FIG 3.1: Cartoon of a simulation with clones implemented. The leftmost image depicts an early time interval after the initially random Voronoi tessellation has been relaxed and clones are first marked. The rightmost image shows the tissue after it has grown slightly, demonstrating how cells created from the division of clones inherit its distinct marking so the statistics of their size and growth can be analyzed.

We consider the general anisotropic case for growth only, since divisions in the vertex model are locally anisotropic due to the splitting of cells along specific directions, despite growth appearing isotropic on average. As mentioned in the Chapter I, growth is represented in the continuum model using the second-rank symmetric tensor $G_{ij} = e^{\gamma_0 t}\delta_{ij} + \tilde{G}_{ij}$, where the first term describes a spatially uniform expansion with average growth rate γ_0 at time *t,* and the second term describes fluctuations around this average. The dynamics of $\tilde{G}$ are defined assuming small deviations from uniform growth in terms of the stress tensor, given by

$$\partial_t \left[\frac{\tilde{G}_{ij}}{\bar{G}}\right] = c\sigma_{ll}\frac{\delta_{ij}}{2} + c^{(d)}\left(\sigma_{ij} - \sigma_{ll}\frac{\delta_{ij}}{2}\right) + \xi_{ij}(\boldsymbol{R}, t)\,. \tag{3.1}$$

This gives the time derivative of growth fluctuations at fixed Lagrangian coordinates $\boldsymbol{R}$, capturing the effects of both stress feedbacks and noise. The constants c and $c^{(d)}$ describe the strengths of feedback on hydrostatic and deviatoric stresses, respectively, and ξ_{ij} is a noise term. (1.6) introduced the expression for density fluctuations, which related $\delta\rho$ to $\tilde{G}$ by two scalar quantities $\tilde{G}_{ll}$ and $\tilde{G}_{\parallel}$. Analogously, we can define a pair of independent, Gaussian random variables $\tilde{\xi}_{ll}$ and $\tilde{\xi}_{\parallel}$ corresponding to the noise associated with these two components of growth. These terms are taken to be delta correlated in space and time.

Substituting an appropriate stress into (3.1) yields differential equations describing dynamics in terms of three independent modes. The two relevant for the analysis of clones are

$$\partial_t \delta\rho = -\left(k + k^{(d)}\right)\delta\rho + \rho_0 \frac{\mu}{\lambda + 2\mu}(\xi_{ll} - 2\xi_{\parallel}) \tag{3.2}$$

$$\partial_t Z_L = \xi_{ll} + 2\frac{k}{k^{(d)}}\xi_{\parallel}\,. \tag{3.3}$$

Here k is a constant written in terms of feedback strength and the Lamé coefficients, $k = \frac{2\mu c(\lambda+\mu)}{\lambda+2\mu}$, and $k^{(d)}$ is the deviatoric analog defined similarly. The second of these equations describe Z_L, the amplitude of the longitudinal soft mode, which produces no stress in the tissue and thus grows diffusively. This soft mode implies that the random fluctuations of growth induce displacements that exactly cancel in such a way that discourages mechanical stress or changes in density, whereby areas of the tissue experiencing faster growth will balance out with areas of slower growth.

These results allow one to define an expression to describe the variance of clone size. Starting with an initially circular clone of radius R_c, this variance is given by the lengthy result

$$var(A) = \bar{G}^4 \int_{\boldsymbol{R}\le R_c}\int_{\boldsymbol{R}'\le R_c}\left[\begin{array}{c}\frac{{\alpha_1}^2}{{\rho_0}^2}\langle\delta\rho(\boldsymbol{R},t)\delta\rho(\boldsymbol{R}',t)\rangle + \frac{2\alpha_1\alpha_2}{\rho_0}\langle\delta\rho(\boldsymbol{R},t)Z_L(\boldsymbol{R}',t)\rangle \\ +{\alpha_2}^2\langle Z_L(\boldsymbol{R},t)Z_L(\boldsymbol{R}',t)\rangle\end{array}\right] d\boldsymbol{R}d\boldsymbol{R}'\,, \tag{3.4}$$

with simplifying constants $\alpha_1 = \frac{(\lambda+\mu)k-\mu k^{(d)}}{\mu\left(k+k^{(d)}\right)}$ and $\alpha_2 = \frac{k^{(d)}}{k+k^{(d)}}$. From (3.2) and (3.3) we see that the autocorrelation terms above will expand into autocorrelation terms for noise. These autocorrelations are defined in the following ways, with fixed noise strengths D_1 and D_2:

$$\langle \xi_{ll}(\boldsymbol{R},t)\xi_{nn}(\boldsymbol{R}',t')\rangle = \frac{D_1}{\bar{G}^2}\delta(t-t')\delta(\boldsymbol{R}-\boldsymbol{R}') \tag{3.5}$$

$$\langle \xi_{\parallel}(\boldsymbol{R},t)\xi_{\parallel}(\boldsymbol{R}',t')\rangle = \frac{D_2}{\bar{G}^2}\delta(t-t')\delta(\boldsymbol{R}-\boldsymbol{R}')\,. \tag{3.6}$$

Using these results from the model, we can now derive the equations which will be applied for the comparison to vertex model simulations. We are interested in finding the behavior of $var(A)$ throughout time, which will involve additional integrations of (3.4) with respect to time. After expanding the correlators of (3.4), substituting in (3.5) and (3.6), and integrating over space and time, we can construct an expression describing the variance of clone sizes compared with the mean,

$$\frac{var(A)}{\langle A\rangle^2} = \frac{1}{\pi {R_c}^2}\left[\mathrm{A}(e^{-2\gamma_0 t}-e^{-2kt}) + \mathrm{B}(e^{-2\gamma_0 t}-e^{-kt}) + C(1-e^{-2\gamma_0 t})\right], \tag{3.7}$$

where the mean area is given by $\langle A\rangle = \bar{G}^2\pi {R_c}^2$, and the prefactors by

$$\mathrm{A} = \frac{1}{2}\frac{(\lambda+\mu)^2}{(\lambda+2\mu)^2}\frac{D_1+4D_2}{k-\gamma_0} \tag{3.8}$$

$$\mathrm{B} = -2\frac{\lambda+\mu}{\lambda+2\mu}\frac{4D_2}{k-2\gamma_0} \tag{3.9}$$

$$C = \frac{2D_2}{\gamma_0}\ . \tag{3.10}$$

This result is taken in the limit where $k^{(d)} \to 0$, since although the vertex model allows *random* deviations from isotropic growth arising from the anisotropy of individual cell division evens, we

consider here a mechanical feedback, as will soon be discussed, that effects growth in an isotropic manner. At long times, it is clear from (3.7) that the variance will approach a constant, and scale like initial clone size,

$$\lim_{t\to\infty}\left(\frac{var(A)}{\langle A\rangle^2}\right)=\frac{2D_2}{\gamma_0\pi {R_c}^2}\sim\frac{1}{{R_c}^2}\,. \tag{3.11}$$

This tells one that the variability of clone size depends only on the size of the initial clone, and surprisingly, not on the size of the clone at any given point in time. This result is unique to the case of anisotropic growth due to the soft mode dynamics, as this ratio decays to zero for the isotropic case for which soft modes are not present. Equations (3.7) and (3.11) will be tested against the variance of clone areas in simulations to determine if predictions from the continuum model accurately translate to results from our discretized model.

3.2 Parallels to the Vertex Model

To create simulations that can be compared to the continuum model, a pressure dependent mechanical feedback was added to the vertex model that regulates cell division rates. Mitosis can occur at each time interval during the simulations, where each cell is given a small probability p_0 to divide, creating a new edge that splits its area in half along a random direction and imparting its properties to two daughter cells. A feedback meant to isotropically damp density fluctuations where they occur is implemented by introducing a linear pressure dependence to this initial division probability, where pressure in the model is defined for cell *i* using $P = K(A_0 - A_i)$. This is meant to affect growth such that the probability of division at a given time interval is higher for cells above their preferred area than cells below,

$$p = p_0\left[1-\frac{P}{KA_0(1-f)}\right], \tag{3.12}$$

where *f* is a parameter that sets the strength of the feedback. This choice in feedback describes a simple linear dependence on pressure, where any cell a fraction *f* of the preferred area will have

zero chance to divide, a cell satisfying its preferred area will divide with probability p_0, and a cell above this will have an increased chance to divide. For any cell below the area threshold of fA_0 that would produce a negative probability from (3.12), we manually set $p = 0$. Although it was also implemented that a cell is given an associated probability to activate cell death below this threshold, cells under this area rarely occurred using standard parameters and so had a negligible effect on simulation results. In this respect, *f* is chosen such that $0 < f < 1$, where values close to 0 correspond to lower feedback strengths, and values close to 1 are higher in strength – choices for *f* outside these bounds cease to have physical meaning and are not considered.

Next, we consider how to relate the parameters in the vertex model describing growth and feedback with those involved in the continuum model. For growth, this means finding a way to express the uniform growth constant γ_0 in terms of the fixed probability assigned to each cell for division, p_0. We will do this by comparing how the total area of the tissue should evolve in either case. For the continuum model, the dilation of a tissue starting at an area of A_0 is given by $A_0 e^{2\gamma_0 t}$, whereas growth in the discretized model can be represented probabilistically using $A_0(1 + p_0)^t$, where *t* is interpreted as an arbitrary dimensionless unit of time within the simulations. Setting these two expressions equal gives the desired relationship as $2\gamma_0 = \ln(1 + p_0)$. We will find that this result agrees nicely with estimates of the growth rate from simulations.

To find a similar expression for mechanical feedback *k* requires that we first find one for the feedback strength constant mentioned earlier, *c.* If we assume a similar pressure dependent feedback in the continuum as was suggested in (3.12), we can expect growth of the form $\gamma = \gamma_0 - cP$. As explained above, when the pressure of a cell is at some threshold defined by *f* (or when some point $\boldsymbol{R}$ reaches some threshold stress in the case of a continuous elastic sheet), we expect the local growth rate to vanish, such that we can substitute in the previously given definition of pressure to obtain $c = \frac{\gamma_0}{[KA_0(1-f)]}$. This allows us to make a theoretical estimate for *k* based on parameters all attainable from the vertex model itself,

$$k = \frac{\lambda + \mu}{\lambda + 2\mu} \frac{2\mu\gamma_0}{KA_0(1 - f)} \ . \tag{3.13}$$

Using the standard parameter choices for *K,* A_0, γ_0 derived above, and the results from Chapter II to describe the Lamé coefficients, the feedback strength of the simulations should be determined by our choice in *f*.

3.3 Results and Conclusion

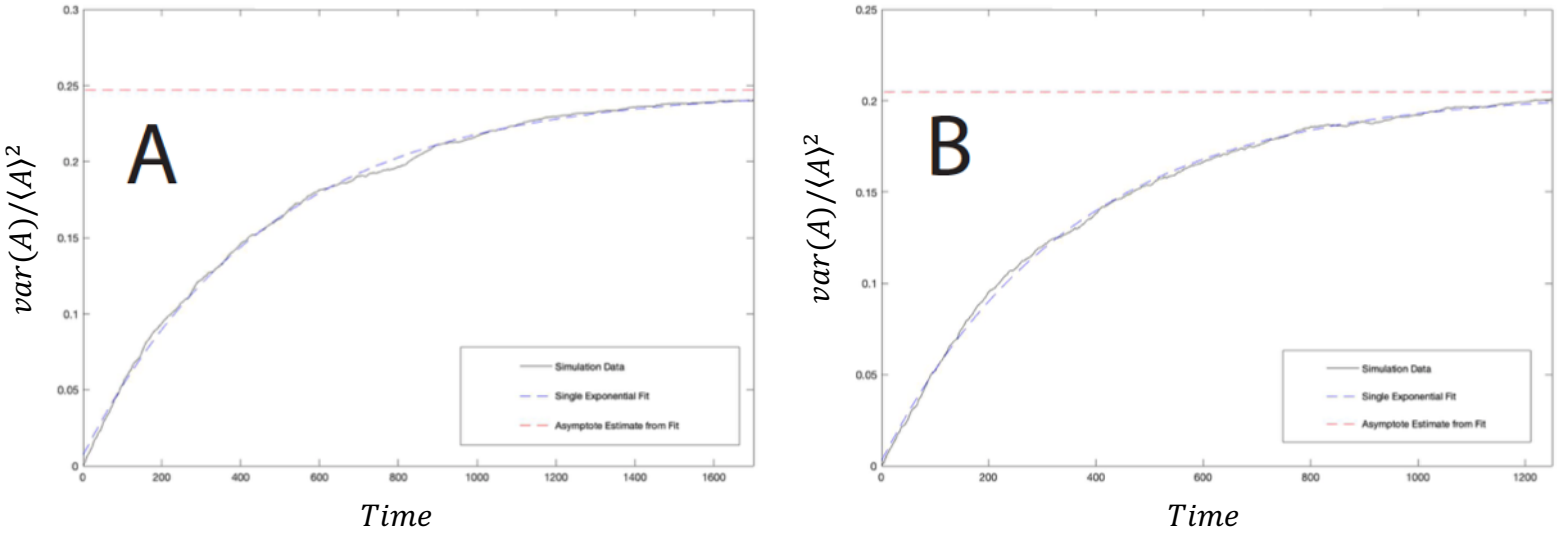

FIG 3.2: $var(A)/\langle A\rangle^2$ as a function of time intervals for different choices of feedback strength. The dashed blue curve fits the data to a single exponential function of the form $g_1(t) = c_1 - c_2 e^{-c_3 t}$. The red dashed line represents an estimate of the asymptote based on the fit. **A** No feedback implemented into the simulation. **B** A case of stronger feedback strength, such that $f = 2/3$.

The simulations used for the following results begin with an initially random Voronoi tessellation of 250 cells and divide until the packing reaches a size of 10^4 cells – a number chosen so that dynamics may be reasonably compared with those assuming an infinite tissue. We use the standard parameter set for Γ and *K* and assume the estimated bulk and shear properties of the tissue found in Chapter II. The probability of a cell dividing per time interval is chosen such that the tissue grows quasistatically, in this case with a chance of $\frac{1}{400}$, so that $2\gamma_0 = 0.002497$. The values of *f* used, in ascending order of strength, are $\frac{1}{3}$, $\frac{2}{3}$, and $\frac{9}{10}$, chosen such that the scale of k is comparable to that of γ_0. The case where mechanical feedback is not included is also considered. At the beginning of the simulations, 20 groups of cells are chosen of some initial size, and each

marked uniquely such that their progeny inherit this mark. An example of a group of clones evolving in time is shown in fig. 3.1. The statistics for clones was taken by averaging data over 100 different simulations, amounting to 2000 clones.

Fig 3.2 shows two examples of the behavior of $var(A)/\langle A\rangle^2$. For every choice of feedback strength tested, the plots demonstrate a clear asymptotic trend at large times, as predicted to occur from the presence of soft modes in the anisotropic case of growth. Two different strategies were employed to fit the simulation data. Both sets of fits were performed using the MATLAB (R2017b) nonlinear least-squares curve-fitting function *lsqcurvefit.* The first of these fits uses a generic set of exponential functions to match the form of (3.7), the resultant fitted parameters for which are shown in Table 3.1. We found that for any choice of feedback strength, the best fit was provided using a single exponential function of the form $g_1(t) = c_1 - c_2 e^{-c_3 t}$. In fact, we see that for every feedback strength tested, $c_1 \approx c_2$, which suggests that each roughly assume the form of (3.7) in the case of no feedback when $k \to 0$,

$$\lim_{k\to 0}\left(\frac{var(A)}{\langle A\rangle^2}\right) = \frac{\mathrm{A} + \mathrm{B} - C}{\pi {R_c}^2}\left[e^{-2\gamma_0 t} - 1\right]. \tag{3.14}$$

As seen in Table 3.1, the fitting parameter in the exponent for g_1 consistently agreed with our expectations for the growth rate. Without feedback, this parameter was estimated to be $c_3 = 0.002511$, closely resembling the theoretical estimate of $2\gamma_0$. Including feedback, the fitting parameter never exceeded a percent error of 14% of the expected value. However, disagreements begin to surface when a second or third exponential is added to the fits where we expect to see fitted exponents that resemble our predictions for growth rate *and* feedback strength. In every case, the fitting parameters in the exponents were nearly identical, suggesting that the data is best fit with a single exponential function. This implies that the variance curves seem to neglect the effects of feedback and are modeled best accounting only for the contributions from growth rate.

f	k	c_1	c_2	c_3	c_4	c_5
$g_1(t) = c_1 - c_2 e^{-c_3 t}$						
	0	0.2402	0.2470	0.00251		
$1/3$	0.000190	0.2297	0.2250	0.00243		
$2/3$	0.000380	0.2048	0.2023	0.00284		
$9/10$	0.001265	0.1489	0.1509	0.00255		
$g_2(t) = c_1 - c_2 e^{-c_3 t} - c_4 e^{-c_5 t}$						
	0	0.2075	0.0795	0.00298	0.0901	0.00299
$1/3$	0.000190	0.1865	0.0708	0.00380	0.0982	0.00381
$2/3$	0.000380	0.1799	0.0908	0.00338	0.0614	0.00342
$9/10$	0.001265	0.2049	0.0764	0.00308	0.0912	0.00310

Table 3.1: Displayed in each row is the ratio *f* determining feedback strength, the corresponding value for *k* estimated using the standard parameter set, and the coefficients from different exponential fits $g_1(t)$ and $g_2(t)$. For g_1, the estimate for c_3 closely resembles our predictions of $2\gamma_0$. For g_2, the columns for c_3 and c_5 represent the fitted exponents. The similarity of these two estimates in each case suggest that the data is better modeled by a single exponential function. The fits for a function with three exponentials are omitted for space since it suggests the same conclusion as the double exponential.

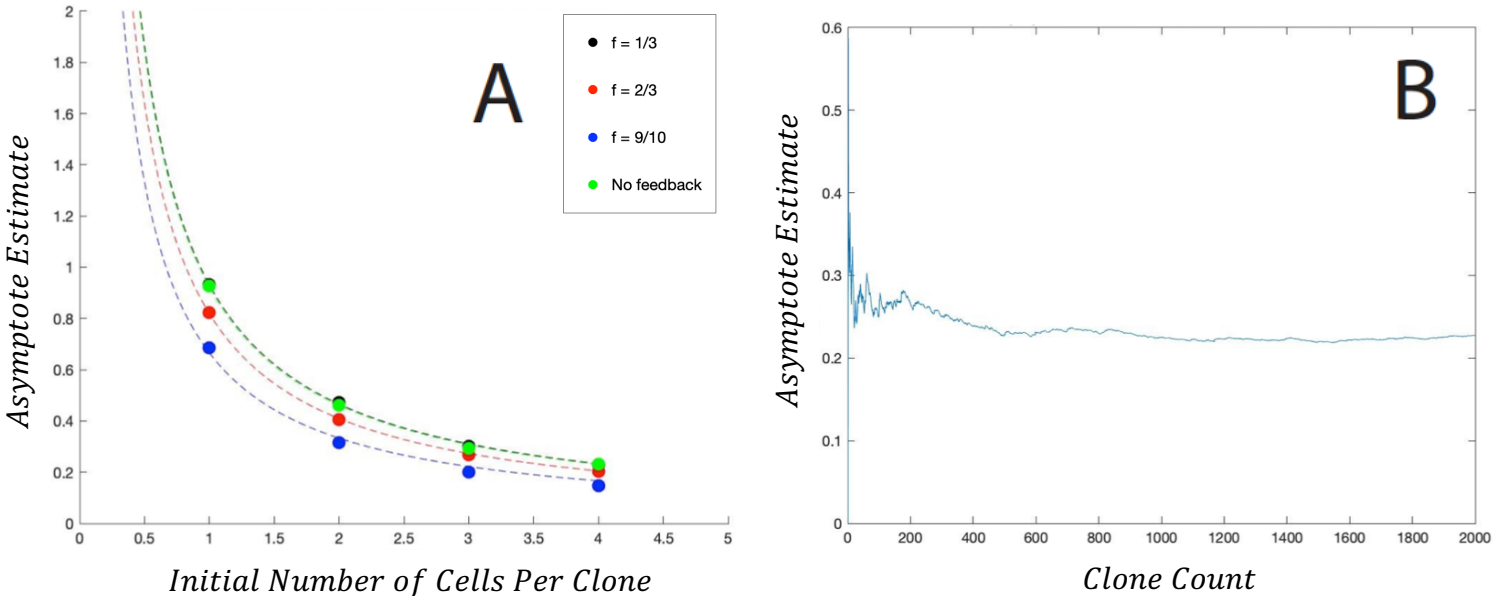

FIG 3.3: **A** The estimate of the asymptote of $var(A)/\langle A\rangle^2$ for $t \to \infty$, extracted from single exponential fits (as in fig. 3.2) for clones of varied initial sizes. We show results for different feedback strengths and see that all obey the same $1/n_c$ behavior demonstrated by the fits, where n_c is the initial number of cells per clone. **B** We show how estimations of the asymptote vary as a function of the number of clones analyzed for an arbitrary case of feedback strength (no feedback, in this case). We see that using 2000 clones converges to a stable value.

We now consider the dependence of the clone size variance with their initial area, as proposed in (3.11). This was done by taking the asymptote estimates using the single exponential fits described above, where the initial number of cells in a clone range identically in each case from 1 to 4. The values of these asymptotes are plotted against initial clone size, as shown in fig. 3.3 (a). If we assume the number of cells in a clone scales closely with its total area, we then see that the data demonstrates a clear inverse relationship between the clone variance as $t \to \infty$ and its initial area. This verifies the basic relationship proposed in (3.11), implying that the variance of a large clone's area is just as much as a smaller clone, depending only on the initial size that each starts out as. There also appears to be a systematic decrease in variance as feedback increases, though the clone area dependence is correctly maintained between all cases. The apparent feedback dependence displayed by the curves, although intuitive to suspect that variance should decrease with increased k, is an unexpected result of its long-term behavior.

The second set of fits were taken assuming all the estimated parameters from the vertex model, where the only unknowns are the noise constants, D_1 and D_2. The same nonlinear least-

squares fitting function was applied on the variance data to model (3.7) exactly, using the noise constants as fitting parameters. The details of these fits can be viewed in Table 3.2, and clearly reflect the incompatibility between clone behavior found in the vertex model and that predicted for the continuum. The asymptotes at large *t* suggested by these fits are inconsistent with that seen in the data. Further, the noise constants appear to have some unexpected correlation with *k*, which should remain constant between different instances of feedback.

f	k	D_1	D_2	*Asymptote Estimate*
	0	0.6795	0.3183	0.4079
$1/3$	0.000189	0.3820	0.9431	1.2087
$2/3$	0.000380	0.6175	0.5105	0.6542
$9/10$	0.001265	1.1434	0.2716	0.3480

Table 3.2: Displayed in each row are the results from fitting $var(A)/\langle A\rangle^2$ for different feedback strengths using D_1 and D_2 as fitting parameters. We see that D_1 and D_2 appear to vary with k, which are expected to remain constant. Also showed are the estimates for $var(A)/\langle A\rangle^2$ as $t \to \infty$, which are much higher than what the data suggests it should be. This table implies that the continuum model does not accurately reflect the clone variance from the simulations.

These results suggest that the clones in simulations are demonstrating dynamics not fully captured from those described of a continuous elastic sheet. Though we can observe certain predictions that are relevant to the simulations – namely, the dependence of size variance on initial clone size and the apparent asymptotic behavior of these curves because of soft modes unique to anisotropic growth – it appears that the effects of mechanical feedback are largely neglected in the vertex model despite this. It is likely the case that the simulations are displaying certain nonlinear behaviors during its evolution related to the presence of hyperuniformity, as seen in Chapter II, negating the effects of any implemented feedback. The formulations of the Damavandi and Lubensky paper are those of a linear elastic continuum, and the suppression of density fluctuations is not supported outside of those induced by an added mechanical feedback. It is prudent, then, to develop a full understanding of hyperuniformity before returning to the subject of this chapter further. Recent progress and efforts to do this will be the focus of Chapter IV.

CHAPTER IV
Developing New Models

In light of results from the previous two chapters, it should be evident that the recurrence of hyperuniformity in the current state of the vertex model is an anomaly which cannot be ignored. The conclusions of Chapters II and III suggest that the suppression of density fluctuations originate from some unexpected nonlinear behavior affecting the dynamics of tissue simulations whether its relaxing with or without cell divisions. Without a means of identifying its cause, it would be ill-advised to apply our model broadly to other physical or theoretical systems describing epithelia, which generally assume some linear elastic properties of the material [27,28]. The set of hurdles elaborated on in Section 2.4 motivates the transition to a new model to expand on the relationship between the manifestation of hyperuniformity in cell networks and its elastic properties. The subject of this chapter, then, is to present the most recent efforts made to develop a new model for this purpose.

We will discuss a model involving a triangular lattice connected by a 2-spring network with uniformly distributed rest lengths. It will be explained how one can measure density fluctuations by how well each triangle conforms to a preferred area based on the rest lengths of its edges, and how the stiffness of both types of springs in the model can alter the bulk and shear properties of the system. The relationship between these stiffness parameters and the moduli will be derived analytically and show results of density fluctuations for various ratios of μ/κ. We find that results do not appear hyperuniform as $\mu/\kappa \to 0$, instead demonstrating Poisson behavior in every case [34]. It should be stressed that this model is not intended as an analogue for epithelia, but rather as a generalization to examine the occurrence of hyperuniformity in elastic systems with quenched randomness. We finish the chapter with a brief proposition of a model to investigate hyperuniformity for future projects.

4.1 Triangular Lattice Model

Choosing a new model to study density fluctuations in place of the vertex model must satisfy a set of requirements that compensates for the limitations inherent in a more

computationally rigorous model, as are conventionally used for the study of epithelia. First, it should simplify dynamics to be more computationally efficient and exhibit the basic properties of an elastic sheet, but still demonstrate an ability to arrange itself in a way that can be generalized and applied to disordered materials. Second, these rearrangements should behave such that a measure of density fluctuations analogous to those for a cellular tissue is clearly defined, and that the bulk and shear properties of the material can be intentionally augmented via the parameters involved in dynamics. Lastly, we want to ensure that the hyperuniformity is a result of nonlinear elastic deformations, and not from flow or plastic deformations. Thus, we want to see hyperuniformity in a model without topological changes or opportunities to flow, such as T1's.

We propose a model satisfying each of these constraints, referred to here as the *Triangular Lattice Model.* Fundamentally, the components are the same as those used in the vertex model, insofar that we work within a two-dimensional network of cells, edges, and vertices. Forces due to cell pressure and edge tensions, however, are removed and replaced by edges that behave like simple Hookean springs of given rest length l_{0i} and stiffness Γ_i. The energy functional of this network can then be described by

$$U = \sum_i \Gamma_i (l_i - l_{0i})^2 \ . \tag{4.1}$$

The force imposed on each vertex, derived in the same fashion as Section 1.1, thus depends only on the lengths of each edge,

$$F_{\boldsymbol{r}_0} = -\frac{\partial U}{d\boldsymbol{r}_0} = 2 \sum_{[i]} \Gamma_i (l_i - l_{0i}) \widehat{\boldsymbol{l}_i} \ . \tag{4.2}$$

Whereas before cells and vertices could have as many edges or connections as was conducive for reaching a minimal energy configuration, this model (as implied by its name) is initially constructed as a regular triangular lattice, where each vertex is connected by an edge to its nearest neighbor. Topological transitions of any kind are not included, which means major cell rearrangements cannot occur, cells maintain the same three edges initially assigned to them, and

all vertices are three-fold coordinated. Reducing the model to a spring lattice and removing topological changes serves to drastically increase the computational efficiency of the system.

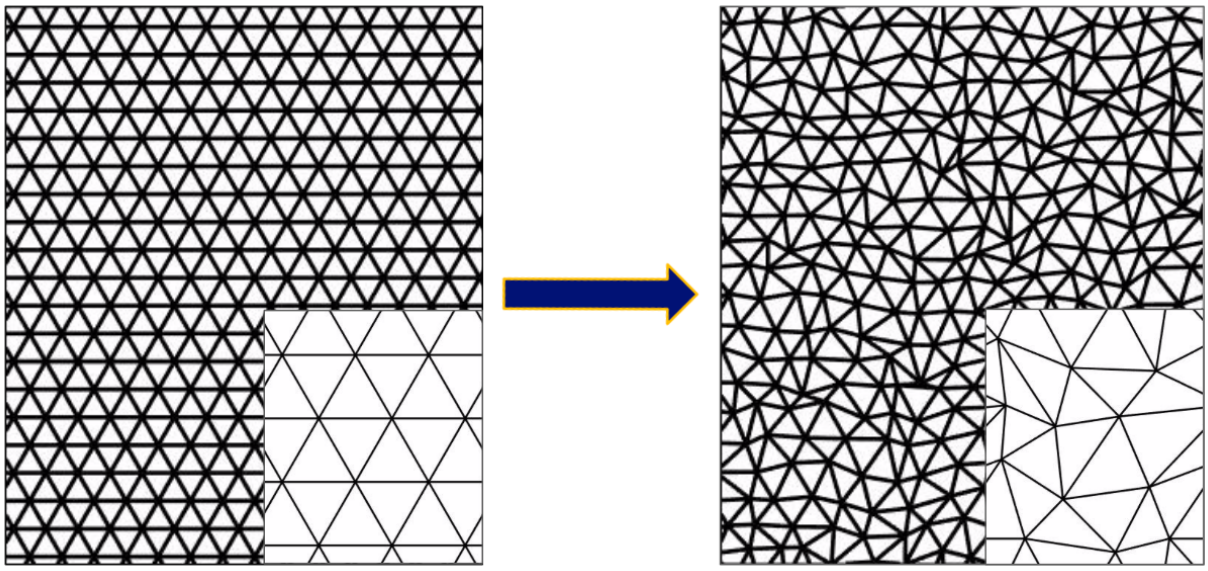

FIG 4.1: Cartoon showing the evolution of the triangular lattice model simulations. Starting from a regular triangular lattice connected by springs with randomly assigned rest lengths, the triangles warp their shapes to conform with a preferred area set by these rest lengths. Smaller versions of these lattices are shown in either corner for detail.

If we begin with a regular triangular lattice, then for the packing to display some interesting behavior outside of this initially stable configuration, we must implement some variety in either the rest lengths or stiffness of each spring. For this model, we do both. We first discuss rest lengths, which are assigned randomly to each edge and meant to introduce some amount of disorder to the packing. In this respect, l_{0i} acts as a random variable distributed uniformly about the characteristic length of an edge in the regular triangular lattice, l_0. Assigning random rest lengths means that a unique preferred area can be calculated for each triangle given the assignment of its three edges. Geometrically, this corresponds to the existence of some target background metric for the lattice, such that the initial regular configuration represents a heterogeneous distribution of area and experiences random local stresses [44]. For large enough packings, the preferred area of all triangles is expected to match that of the box, preventing any complications of internal stresses

resembling a net pressure inflicted on the system. This implies that there exists an equilibrium configuration the lattice can relax to that conforms to each triangle's preferred area, effectively resulting in a packing of uniform density. Thus, we have a new way to measure density fluctuations for the triangular lattice model. By assigning random rest lengths to each edge, one can define a unique preferred area to each triangle, and determine density fluctuations in much the same way as was proposed in eq. (1.5),

$$\langle \delta^2 A_{0i} \rangle = \langle A_{0i}(R)^2 \rangle - \langle A_{0i}(R) \rangle^2 \, . \tag{4.3}$$

This is done by measuring the area of triangles inside an ensemble of measuring windows, with respect to their preferred areas, rather than actual area. By doing this, we can produce plots analogous to those from Chapter II and interpret them in much the same way.

Another feature of the triangular lattice model is that it implements two distinct types of springs of differing stiffnesses. The first type of spring is distinguished by a characteristic stiffness Γ_1, and is assigned a set of edges that together form a honeycomb lattice within the packing. The remaining edges of the triangular lattice are the second type of spring, with characteristic stiffness Γ_2, as shown in fig. 4.2. The choice to include two types of springs was made as a means of manually augmenting the bulk and shear properties of the lattice. For example, setting $\Gamma_2 = 0$ neutralizes the contribution of type 2 springs, reducing the system to a honeycomb lattice, which is known to have zero shear modulus. Conversely, increasing the stiffness of type 2 springs should make the more lattice more rigid and increase its resistance to shear. We then expect density fluctuations to demonstrate the same relationship to the elastic properties of the spring lattice in much the same way we predict it should for the vertex model. To verify these predictions, we must first derive the relationship between the stiffness parameters and elastic moduli of the lattice.

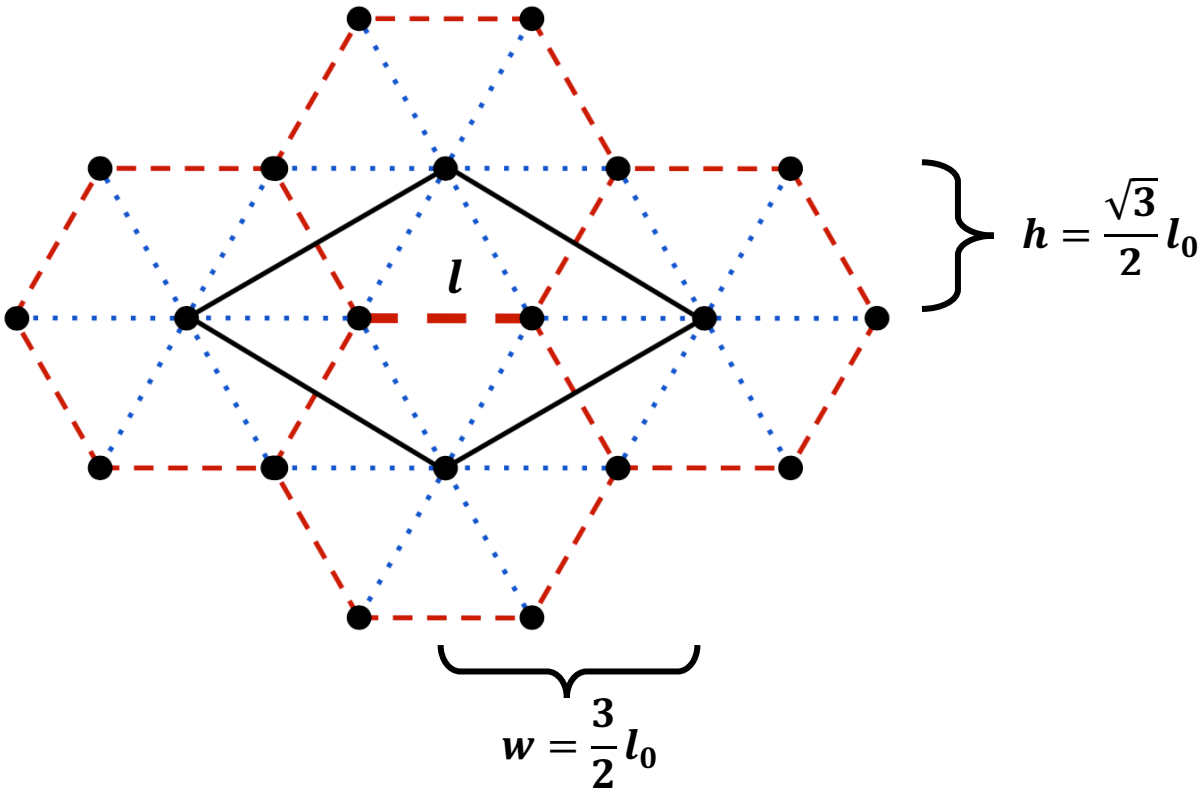

FIG 4.2: Cartoon of the 2-spring lattice in a uniform configuration. *Type 1* springs are shown in red, and here it is clear that together they form a honeycomb lattice. *Type 2* springs are shown in blue. Giving type 2 springs a nonzero stiffness can improve the shear resistance of the system. A unit cell containing two vertices is drawn using black lines, which is used to derive the shear modulus in Section 4.2. The length of the type 1 spring bolded and oriented parallel to the x-axis in the unit cell is used as an energy minimizing parameter, labelled l. We also define quantities of width and height to simplify calculations – w and h in the diagram.

4.2 Elastic Properties of the Lattice

Deriving the relationship between the bulk and shear moduli with respect to Γ_1 and Γ_2 can be done very similarly as was detailed in Section 2.3, though with a spring lattice, this can be done analytically for the case without any randomness. In actuality, the bulk and shear moduli randomly fluctuate in space due to the heterogeneity introduced into the lattice from the variable rest lengths, though these calculations represent the estimated average elastic properties over the entire lattice, valid for large packings.

To calculate the bulk modulus, we can model the energy of the system after applying a hydrostatic deformation by expanding out (4.1) in terms of a packing with m_1 type 1 springs, m_2 type 2 springs, and a scaling factor for the deformation α,

$$E_d^{(\kappa)} = m_1\Gamma_1(\alpha l_0 - l_0)^2 + m_2\Gamma_2(\alpha l_0 - l_0)^2\,, \tag{4.4}$$

where the subscript *d* refers to this representing a discretized form of free energy. We can easily compare this to the continuous elastic expression for free energy in (2.5) to obtain an expression for the bulk modulus. Rewriting $m_1 = 3n$, $m_2 = 6n$, and $L_X L_Y = \left(\frac{3\sqrt{3}}{2} {l_0}^2 n\right)$ in terms of the number of hexagons in the type 1 spring honeycomb, *n*, we find that

$$\kappa = \frac{\sqrt{3}}{3}[\Gamma_1 + 2\Gamma_2]\,. \tag{4.5}$$

The shear modulus proves a bit more difficult to find analytically. To simplify matters, we look at a single unit cell of the lattice containing two vertices, shown in fig. 4.2. To simplify notation, we define a unit of width $w = \frac{3}{2} l_0$ and height $h = \frac{\sqrt{3}}{2} l_0$. We attempt to model the energy of the system after shearing the lattice using a squeeze deformation to find μ. Unlike the bulk modulus, though, we must allow the vertices to move after deforming to find its minimal energy configuration. Taking advantage of symmetries, one recognizes that the vertices will remain bound to the x-axis, so we can parametrize the energy within the unit cell using the length of the edge connecting the two vertices, denoted l. Rewriting the scaling factor $\alpha = \varepsilon + 1$, we can write represent the energy within the unit cell after applying a shear strain $\varepsilon \ll 1$ with respect to l,

$$\begin{aligned} E(l)_d^{(\mu)} = {} & \Gamma_1(l - l_0)^2 + 2\Gamma_1\left(\sqrt{\left(l - \tfrac{w}{\varepsilon+1}\right)^2 + (h[\varepsilon+1])^2} - l_0\right)^2 \\ & + 2\Gamma_2\left(\left[\tfrac{1}{\varepsilon+1} - \tfrac{l}{2}\right] - l_0\right)^2 + 4\Gamma_2\left(\sqrt{\left(\tfrac{l}{2}\right)^2 + (h[\varepsilon+1])^2} - l_0\right)^2\,. \end{aligned} \tag{4.6}$$

Defining the energy in terms of l allows us to minimize energy with respect to l to find the desired configuration. We write l into a power series and expand terms about $\varepsilon = 0$ to second order. Solving $\frac{\partial E(l)_d^{(\mu)}}{\partial l} = 0$ for l thus gives a minimum energy configuration when the edge between the vertices is a length of

$$l^\star = l_0 \left[1 - \frac{3\Gamma_2}{2\Gamma_1 + \Gamma_2}\varepsilon + \frac{3\Gamma_1\left(8{\Gamma_1}^2 - \Gamma_1\Gamma_2 + 11{\Gamma_2}^2\right)}{2(2\Gamma_1 + \Gamma_2)^3}\varepsilon^2\right] . \tag{4.7}$$

We then substitute this result into (4.6) to find the relaxed energy of the unit cell after imposing a squeeze deformation to second order in the strain,

$$E_d^{(\mu)} = {l_0}^2 \left[\frac{3}{2}\Gamma_1\beta^2 + \frac{5}{4}\Gamma_2(\beta - 3)^2\right]\varepsilon^2 , \tag{4.8}$$

where $\beta = \frac{3\Gamma_2}{2\Gamma_1 + \Gamma_2}$. It should be noted that $E_d^{(\mu)} \to 0$ as $\Gamma_2 \to 0$, which is good since we expect energy to vanish to quadratic order for small shear strain in a honeycomb lattice.

Having acquired a discretized expression of free energy, one need only compare this to (2.6) in terms of ε to find the shear modulus. Defining the volume of the continuous elastic formulation $L_X L_Y = \frac{3\sqrt{3}}{2}{l_0}^2$ as that of the unit cell, we find that

$$\mu = \frac{\sqrt{3}}{9}\left[\frac{3}{2}\Gamma_1\beta^2 + \frac{5}{4}\Gamma_2(\beta - 3)^2\right] . \tag{4.9}$$

(4.5) and (4.9) become a system of equations we can use to find Γ_1 and Γ_2 in terms of the moduli, such that $\frac{\mu}{\kappa}$ can be manually chosen for specific choices of the stiffness parameters. The ratios and corresponding choices in parameter used for simulations are shown in Table 4.1. However, it should be noted that given the limit behavior of the moduli, there is an apparent maximum ratio that can be achieved within the constraints of this model. One can show by writing $\frac{\mu}{\kappa}$ in terms of the ratio of the stiffness parameters $\frac{\Gamma_2}{\Gamma_1}$, seen in fig. 4.3 (b), that this max ratio is $\frac{\mu}{\kappa} =$

0.730. The triangular lattice model, then, can modulate the ratio of the moduli to a much higher degree than that demonstrated by the vertex model.

Γ_1	Γ_2	κ	μ	μ/κ
1.7320	0	1	0	0
1.4878	0.1221	1	$1/4$	$1/4$
1.1971	0.2675	1	$1/2$	$1/2$
1.0062	0.3629	1	$5/8$	$5/8$

Table 4.1: Displayed in each row is the parameter schemes used to produce the $\langle \delta^2 A \rangle$ curves in fig. 4.3 (a). We show the choices of parameter required for desired bulk and shear moduli. The parameter schemes are arranged in order of increasing μ/κ.

4.3 Results and Future Direction

Fig. 4.3 (a) shows the density fluctuations of the triangular lattice simulations for different ratios of $\frac{\mu}{\kappa}$. These results were collected from an average of 10 relaxed packings of $6 \cdot 10^4$ triangles, with rest lengths assigned using a uniform distribution over a range of $l_0 \pm \frac{1}{4} l_0$. This range was chosen arbitrarily, since changing it did not seem to have a significant impact on the data. Surprisingly, the density fluctuations are not suppressed for decreasing moduli ratios, in stark contrast to the vertex model case considered in previous chapters. In fact, the plot implies that for any choice of $\frac{\mu}{\kappa}$, the distribution of area throughout the packings are random.

Although a promising start towards developing a model that can illuminate further the relationship between the occurrence of hyperuniformity and the elastic quantities of a disordered material, the data reveals one glaring problem which largely hinders its usefulness. First, to choose values of $\frac{\mu}{\kappa}$ small enough to expect hyperuniform behavior, one of the stiffness parameters must be significantly smaller than the other. A consequence of this is that the forces produced by these springs are, in effect, negligible compared to the other type of springs. This makes it so the triangles can no longer preserve their preferred area, which undermines the

method employed to measure density fluctuations, and tends triangles to adopt a random area. Without knowing if the triangles are unable to conform to their preferred areas due to the bulk and shear constraints imposed on them or from one type of spring dominating dynamics means that very little conclusive information can be extracted from the data. Although they may all have the same slope behavior in fig. 4.3 (a), we do see a systematic decrease in $\langle \delta^2 A \rangle / R^2$ between each of the curves. This is because as $\frac{\mu}{\kappa}$ increases, the stiffness of both types of spring become closer in value, the forces imposed by each are then comparable, and so the triangles can meet their preferred areas to some extent. Although this effect is not significant enough to change the density fluctuation behavior in any of these cases, we do see a slight decrease in variance of area as $\frac{\mu}{\kappa}$ increases.

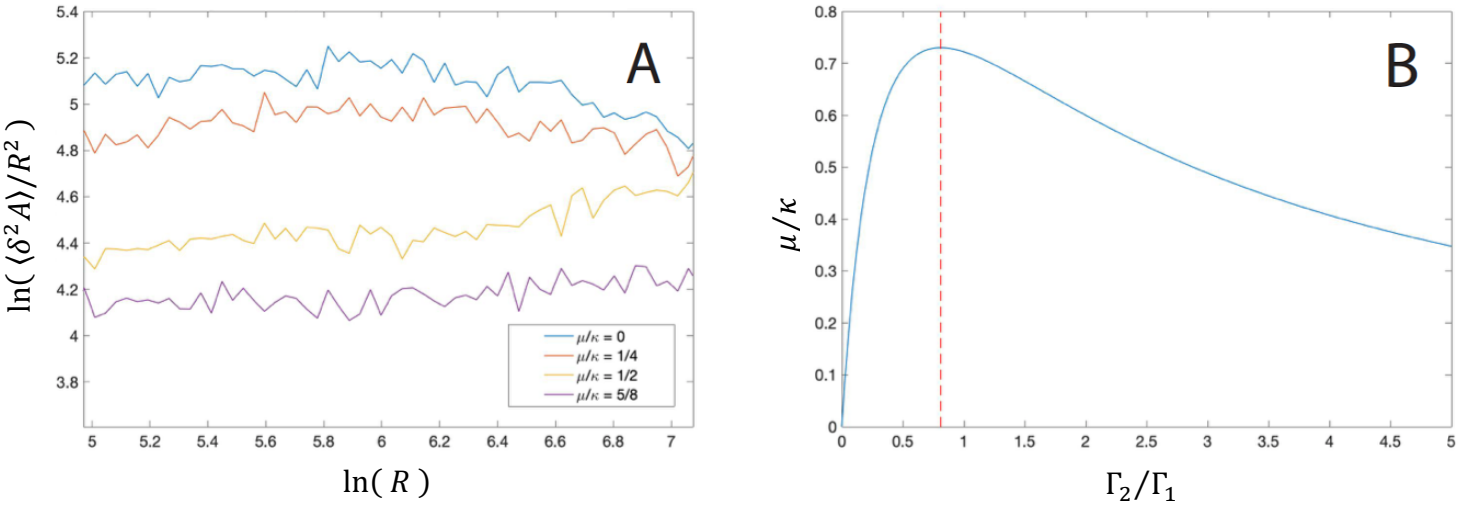

FIG 4.3: **A** Log-log plot of $\langle \delta^2 A \rangle / R^2$ as a function of R for different ratios of μ/κ. The results shown are taken from systems of $6 \cdot 10^4$ triangles, and the bounds of the x-axis have been narrowed to remove data affected by finite size effects, as seen in the plots of Chapter II. The slopes of these curves appear flat, indicating random fluctuations of density in the system in all cases. The only distinction between them is a systematic decrease in the variance of their areas, which is discussed in the text. **B** The blue curve shows the theoretical relationship between μ/κ and the stiffness ratio Γ_2/Γ_1. The red dashed line represents the stiffness ratio that can produce the highest value for μ/κ. This ratio is $\mu/\kappa = 0.730$ for a stiffness ratio of $\Gamma_2/\Gamma_1 = 0.811$. For our data, we choose parameter schemes starting at $\Gamma_2/\Gamma_1 = 0$ and working up towards this maximum.

Current efforts to understand the physical origin of hyperuniformity are in the works, attempting to build off the strategies developed for the triangular lattice model. This involves constructing a new energy functional that penalizes triangles from deviating from a randomly assigned preferred area, along with a spring-like angular dependent energy cost which incentivizes triangles to remain equilateral. Density fluctuations will be measured in largely the same way as described in Section 4.1, though these areas are expected to be preserved due to its explicit definition inside the model. Additionally, we expect that the bulk and shear moduli should be easier to modulate, since they should be coupled independently with the energy contributions generated by deviations from area or bond angles, respectively.

CHAPTER V
Conclusion

In this work, we have detailed the progress regarding the ongoing investigation of anomalous suppression of density fluctuations observed in computational simulations of epithelium. Disordered hyperuniform systems have gained more attention in recent years due to their novel properties and important role in many biological phenomena [31,32,33]. The tools available to study density fluctuations of disordered media at long orders of distance are limited, and efforts to understand the physical mechanisms underlying the presence of hyperuniformity are largely absent. The primary goal of this thesis was to provide insight into the methods used to measure density fluctuations in simulated epithelial tissues and results thereof, as well as develop new models to approach the cause of hyperuniformity observed from a biophysical standpoint. Our investigation regarding the subject has yet to reach a definite conclusion, though the findings presented are interesting in their own respect and establishes a useful groundwork for future courses of study.

Chapter II introduced the vertex model, which allows the simulation and analysis of epithelial tissue by approximating it as a two-dimensional disordered network of cells, edges, and vertices. The dynamics of the resultant cell packings take inspiration from their actual biological structure, accounting for forces due to intrinsic cell pressure and contractile edge tension at cell membranes. We then explained the process of analyze density fluctuations by counting the number of cell centroids within an ensemble of circular measurement windows and plotting the variance of these counts with respect to R, where the behaviors of these curves are used to characterize whether the cell distributions display hyperuniformity. This verified that the simulations demonstrate a clear suppression of density fluctuations using a standard set of parameters chosen to represent the dynamics of *Drosophila* wing discs during early stages of development [38]. We hypothesize that this behavior may relate to physical quantities in the form of the bulk and shear moduli of the material, under the assumption that tissues with a relatively low resistance to shear behave like a fluid and could allow cells the freedom to rearrange necessary to induce hyperuniform configurations. After laying out the technique developed to extract the bulk and shear moduli from our simulations, evidence was shown of this

relationship by comparing the density fluctuations for different ratios of $\frac{\mu}{\kappa}$, though there were many restrictions posed by the vertex model that made further elaboration on these findings infeasible.

Chapter III attempts to lean away from the topic of hyperuniformity and compare simulation data from the vertex model to a recent theoretical continuum model of growth in elastic tissues which accounts for mechanical feedback and noisy dynamics [37]. Here, we formulated expressions allowing certain quantities and predictions from the continuum model to translate compatibly with that of our discretized vertex model in the case of anisotropic growth and implemented an isotropic pressure-dependent feedback regulating division rate. We focused on the statistics of clone size by introducing some of our own into simulations and verified the prediction that for $t \to \infty$, the normalized variance of clone areas scale like the inverse of the initial size of the clone. However, we found that the variance of clone areas through time derived from the continuum model did not correctly predict that demonstrated by simulation data. It is suggestive that the hyperuniformity found in simulations is dampening density fluctuations and undermining the effects of feedback, such that the only simulation data applicable to the continuum model is that which neglects mechanical feedback entirely.

We are then highly motivated to develop new models that can identify the cause of hyperuniformity in the vertex model and disordered, elastic materials in general. Chapter IV suggests our latest attempt for this, in which an initially triangular lattice connected by springs are assigned random rest lengths to implicitly define a preferred area for each triangle. Springs were assigned one of two stiffness parameters with which we could choose to manually alter the bulk and shear properties of the lattice. Although we expected to see a relationship between fluctuations in density corresponding to our choice in $\frac{\mu}{\kappa}$, we found that our method for measuring these fluctuations fail for smaller ratios. This model, however flawed, represents a strong foundation that will be built from in later projects.

Identifying the origins of hyperuniformity poses a difficult challenge to understand given the number of computational obstacles involved. This thesis demonstrates our initial efforts to devise such an understanding, and although our results have varied, each step of progress towards unraveling the questions surrounding hyperuniformity have been useful in their own respect. In addition to presenting evidence of hyperuniform behaviors in simulations of disordered systems, the intention of this thesis is also to serve as a reference for those who might further pursue this

subject within the context of the vertex model in future projects. Our hope is only that with every step, we move closer to realizing the answers we seek.

BIBLIOGRAPHY

1. T. Lecuit, P.F. Lenne (2007) “Cell surface mechanics and the control of cell shape, tissue patterns and morphogenesis” *Nat Rev Mol Cell Biol* 8: 633–644.
2. L.A. Davidson (2008) “Taming the tiger of tissue aggregation: how epithelia control structural assembly of underlying cells” *Dev Cell* 14: 152–154.
3. R. Fernandez-Gonzalez, S. de Matos Simoes, J.C. Roper, S. Eaton, J.A. Zallen (2009) “Myosin II dynamics are regulated by tension in intercalating cells” *Dev Cell* 17: 736–743.
4. M. Osterfield, C. A. Berg, and S. Y. Shvartsman (2017) “Epithelial Patterning, Morphogenesis, and Evolution: Drosophila Eggshell as a Model" *Developmental Cell*, vol. 41, pp. 337-348.
5. M. Rauzi, P.F. Lenne, and T. Lecuit (2010) “Planar polarized actomyosin contractile flows control epithelial junction remodeling" *Nature*, vol. 468, p. 1110.
6. A. M. Greiner, H. Chen, J. P. Spatz, and R. Kemkemer (2013) “Cyclic Tensile Strain Controls Cell Shape and Directs Actin Stress Fiber Formation and Focal Adhesion Alignment in Spreading Cells" *PLOS One*, vol. 8.
7. S. K. Wu, S. Budnar, A. S. Yap, and G. A. Gomez (2014) “Pulsatile contractility of actomyosin networks organizes the cellular cortex at lateral cadherin junctions” *Euro. J. of Cell Biology*, vol. 93, pp. 396-404.
8. H. Kouros-Mehr and Z. Werb (2006). "Candidate regulators of mammary branching morphogenesis identified by genome-wide transcript analysis" *Dev. Dyn*. 235(12): 3404–12.
9. P.A. Raymond, L.K. Barthel, R.L. Bernardos, J.J. Perkowski (2006) “Molecular characterization of retinal stem cells and their niches in adult zebrafish” *BMC Dev Biol* 6: 36.
10. E. Fosslien (2008) "Cancer morphogenesis: role of mitochondrial failure" *Annals of Clinical & Laboratory Science*. 38 (4): 307–329.
11. P. Friedl and J.A. Zallen (2010) “Dynamics of cell-cell and cell-matrix interactions in morphogenesis, regeneration and cancer” *Curr Opin Cell Biol* 22: 557–559.
12. M. Cavey and T. Lecuit (2009) “Molecular bases of cell-cell junctions stability and dynamics” *Cold Spring Harb Perspect Biol* 1: a002998.
13. U. Tepass and K.P. Harris (2007) “Adherens junctions in Drosophila retinal morphogenesis” *Trends Cell Biol* 17: 26–35.

14. J. D. Axelrod (2009) “Progress and challenges in understanding planar cell polarity signaling," *Seminars in Cell & Developmental Biology*, vol. 20, no. 8, pp. 964- 971.
15. A. Classen, K. Anderson, E. Marois, and S. Eaton (2005) “Hexagonal packing of Drosophila wing epithelial cells by the planar cell polarity pathway," *Dev. Cell*, vol. 9, pp. 805-817.
16. M. Spencer (2018) “The role of topology and topological changes in the mechanical properties of epithelia” PhD thesis (Univ of Michigan, Ann Arbor, MI).
17. C. Cadart, E. Zlotek-Zlotkiewicz, M. Le Berre, M. Piel, and H. K. Matthews (2014) “Exploring the Function of Cell Shape and Size during Mitosis" *Developmental Cell*, vol. 29, pp. 159-169.
18. D.L. Weaire, S. Hutzler (1999) “The Physics of Foams” Oxford; New York: Clarendon Press. 246 pp.
19. S. Schilling, M. Willecke, T. Aegerter-Wilmsen, O. A. Cirpka, K. Basler, and C. von Mering (2011) “Cell-Sorting at the A/P boundary in the Drosophila wing primordium: a computational model to consolidate observed non-local effects of Hh signaling" *PLOS Comp. Bio.*, vol. 7.
20. D. Bi, X. Yang, M.C. Marchetti, and M.L. Manning (2016) “Motility-Driven Glass and Jamming Transitions in Biological Tissues” *Phys. Rev. X*, 6, 021011.
21. A. G. Fletcher, M. Osterfield, R. E. Baker, and S. Y. Shvartsman (2014) “Vertex Models of Epithelial Morphogenesis" *Biophys. J*., vol. 106, pp. 2291-2304.
22. A. G. Fletcher, J. M. Osborne, P. K. Maini, and D. J. Gavaghan (2013) “Implementing vertex dynamics models of cell populations in biology within a consistent computational framework" *Progress in Biophysics & Molecular Biology*, vol. 113, pp. 299-326.
23. P. A. Raymond, S. M. Colvin, Z. Jabeen, M. Nagashima, L. K. Barthel, J. Hadidjojo, L. Popova, V. R. Pejaver, and D. K. Lubensky (2014) “Patterning the Cone Mosaic Array in Zebrafish Retina Requires Specification of Ultraviolet-Sensitive Cones" *PLOS ONE*, vol. 9.
24. T. Nagai and H. Honda, (2001) “A dynamic cell model for the formation of epithelial tissues" Phil. *Mag. B,* vol. 81, no. 7, pp. 699-719.
25. S. Ishihara, K. Sugimura, S. J. Cox, I. Bonnet, Y. Bellaïche, and F. Graner (2013) “Comparative study of non-invasive force and stress inference methods in tissue" *Eur. Phys. J.* E, vol. 36, p. 9859.
26. P. Spahn and R. Reuter (2013) “A Vertex Model of Drosophila Ventral Furrow Formation" *PLOS ONE*, vol. 8.
27. N.A. Dye, et al. (2017) “Cell dynamics underlying oriented growth of the Drosophila wing imaginal disc” *Development* 144:4406–4421.
28. M.C. Gibson, A.B. Patel, R. Nagpal, N. Perrimon (2006) “The emergence of geometric order in proliferating metazoan epithelia” *Nature* 442:1038–1041.
29. L.D. Landau, E.M. Lifshitz (1986) “Theory of Elasticity” (Butterworth-Heinemann, Oxford, UK).
30. W. Nowacki (1986) “Thermoelasticity” (Pergamon, Oxford, UK), 2nd Ed.
31. S. Torquato (2018) “Hyperuniform states of matter” *Physics Reports* 745, 1-95
32. S. Torquato and F. H. Stillinger (2003) “Local density fluctuations, hyperuniformity, and order metrics” *Phys. Rev*. E 68, 041113.

33. Y. Zheng, Y. Li, and M.P. Ciamarra (2020) “Hyperuniformity and density fluctuations at a rigidity transition in a model of biological tissues” *Soft Matter*, 2020, 16, 5942-5950
34. A.T. Chieco, R. Dreyfus, and D.J. Durian (2017) “Characterizing pixel and point patterns with a hyperuniformity disorder length” *Phys. Rev*. E 96, 032909.
35. Klatt, M.A., Lovrić, J., Chen, D. *et al.* (2019) “Universal hidden order in amorphous cellular geometries” *Nat Commun* 10, 811.
36. D. Hexner and D. Levine (2017) “Noise, diffusion, and hyperuniformity” *Phys. Rev*. Lett. 118, 020601.
37. O. Damavandi and D.K. Lubensky (2019) *PNAS* 116 (12) 5350-5355
38. G. Salbreux, L.K. Barthel, P.A. Raymond, D.K. Lubensky (2012) “Coupling Mechanical Deformations and Planar Cell Polarity to Create Regular Patterns in the Zebrafish Retina” *PLoS Comput Biol* 8(8): e1002618.
39. S. Rulands, et al. (2018) “Universality of clone dynamics during tissue development” *Nat Phys* 14:469–474.
40. I. Heemskerk, T. Lecuit, L. LeGoff (2014) “Dynamic clonal analysis based on chronic in vivo imaging allows multiscale quantification of growth in the Drosophila wing disc” *Development* 141:2339–2348.
41. A.M. Klein, B.D. Simons (2011) “Universal patterns of stem cell fate in cycling adult tissues” *Development* 138:3103–3111.
42. S. Comertpay, S. Pastorino, M. Tanji *et al*. (2014) "Evaluation of clonal origin of malignant mesothelioma". *Journal of Translational Medicine*. 12 (1): 301.
43. P. Greulich, B.D. Simons (2016) “Dynamic heterogeneity as a strategy of stem cell self-renewal” *Proc Natl Acad Sci USA* 113:7509–7514.
44. B.A. DiDonna and T.C. Lubensky (2005) “Nonaffine correlations in random elastic media” *Phys. Rev.* E 72, 066619.